nature astronomy

Article

https://doi.org/10.1038/s41550-024-02362-0

A magnetized Galactic halo from inner Galaxy outflows

Received: 2 March 2024

Accepted: 12 August 2024

Published online: 23 September 2024

Check for updates

He-Shou Zhang [1] ✉, Gabriele Ponti [1,2] ✉, Ettore Carretti [3] ✉, Ruo-Yu Liu [4,5] ✉, Mark R. Morris [6] ✉, Marijke Haverkorn [7], Nicola Locatelli [1,2], Xueying Zheng [2], Felix Aharonian [8,9,10], Hai-Ming Zhang [4,11], Yi Zhang [2], Giovanni Stel [1,12], Andrew Strong [2], Michael C. H. Yeung [2] & Andrea Merloni [2]

Magnetic halos of galaxies are crucial for understanding galaxy evolution, galactic-scale outflows and feedback from star formation activity. Identifying the magnetized halo of the Milky Way is challenging because of the potential contamination from foreground emission arising in local spiral arms. In addition, it is unclear how our magnetic halo is influenced by recently revealed large-scale structures such as the X-ray-emitting eROSITA Bubbles detected by the extended Roentgen Survey with an Imaging Telescope Array (eROSITA). Here we report the identification of several kiloparsec-scale magnetized structures on the basis of their polarized radio emission and their gamma-ray counterparts, which can be interpreted as the radiation of relativistic electrons in the Galactic magnetic halo. These non-thermal structures extend far above and below the Galactic plane and are spatially coincident with the thermal X-ray emission from the eROSITA Bubbles. The morphological consistency of these structures suggests a common origin, which can be sustained by Galactic outflows driven by active star-forming regions located in the Galactic Disk at 3–5 kpc from the Galactic Centre. These results reveal how X-ray-emitting and magnetized halos of spiral galaxies can be related to intense star formation activities and suggest that the X-shaped coherent magnetic structures observed in their halos can stem from galactic outflows.

X-ray-emitting galactic halos have been discovered in star-forming galaxies[1,2]. Several of them are accompanied by large-scale coherent magnetic structures revealed by radio data[3,4]. These large-scale magnetic fields are observed off the galaxy mid-planes, indicating that these galaxies harbour magnetized halos. However, the relationship between the X-ray-emitting and magnetized galactic halos is unclear, and similarly for their nature and origins. The recent discovery of the large X-ray-emitting structures within the Milky Way halo, the eROSITA Bubbles detected by the extended Roentgen Survey with an Imaging Telescope Array (eROSITA)[5], provides important physical insights that enhance our understanding of galactic halos.

Figure 1 compares the eROSITA all-sky emission at 0.6–1.0 keV with the magnetic field determined from the polarized synchrotron emission at 22.8 GHz from the Wilkinson Microwave Anisotropy Probe (WMAP)[6], for which Faraday rotation effects are marginal. Several magnetic structures revealed through their polarized emission and coherent field line direction, here denoted as magnetic ridges, appear in the inner Galaxy, emerging from the Galactic plane[7] and stretching for more than ±20°. The polarized intensity is enhanced at the edges of the eROSITA bubbles (Extended Data Fig. 1). The magnetic field directions are parallel to the bubbles' edges in the east. The magnetic ridges show a general tilt westwards, starting from the disk and rising to

A full list of affiliations appears at the end of the paper. ✉e-mail: heshou.zhang@inaf.it; heshouzhang.astrophy@gmail.com; gabriele.ponti@inaf.it; carretti@ira.inaf.it; ryliu@nju.edu.cn; morris@astro.ucla.edu

https://doi.org/10.1038/s41550-024-02362-0

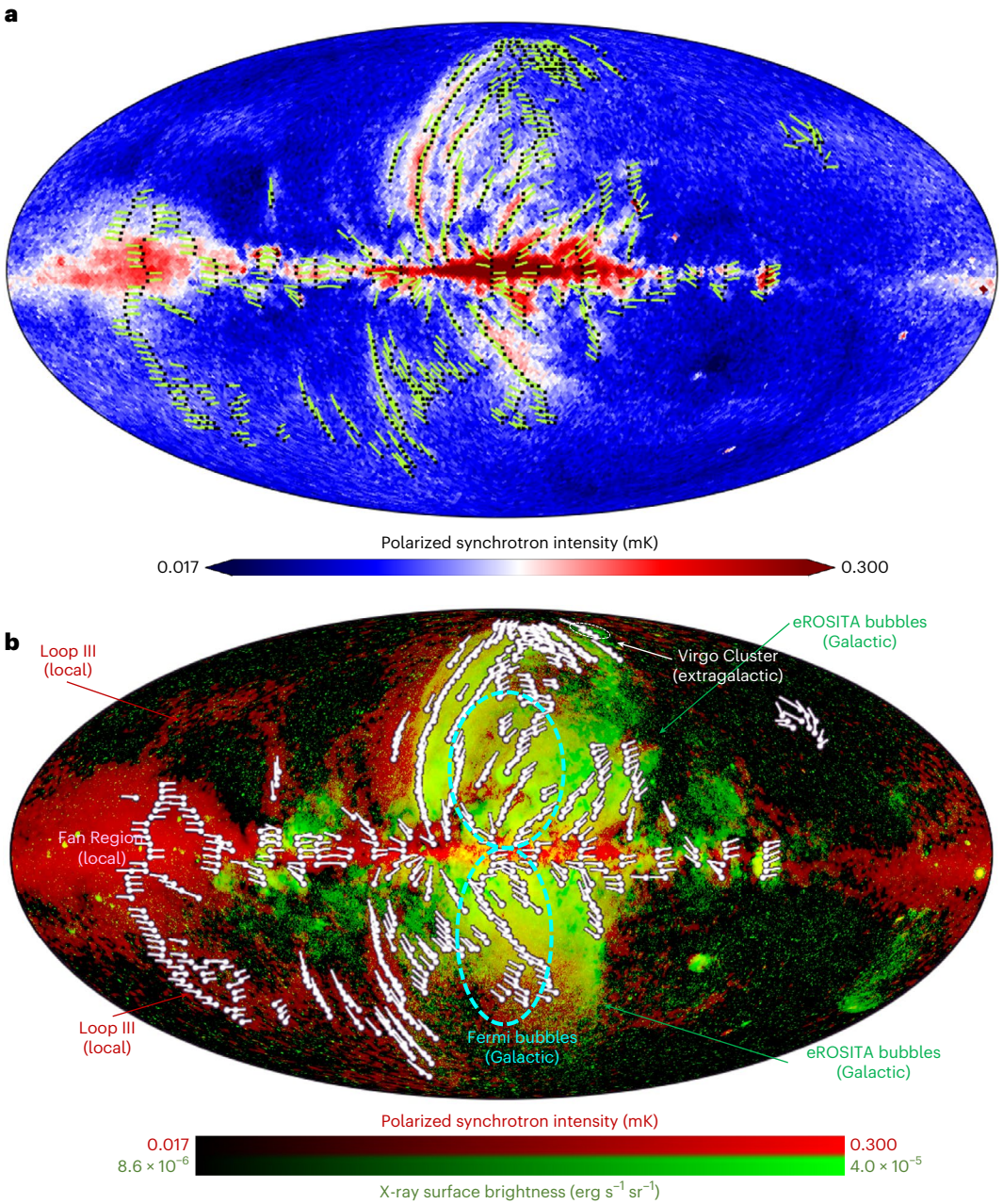

Fig. 1 | Polarized radio counterpart of the eROSITA bubbles. a, Background image showing the polarized synchrotron intensity (PI_{syn}) from WMAP data at 22.8 GHz. Black dots indicate local maxima of PI_{syn} estimated from constant-latitude profiles. Green bars show the magnetic field direction inferred from polarized synchrotron emission. Several coherent magnetized ridges rise from the Galactic Disk and are progressively bent towards the west with increasing latitude. **b**, Magnetized ridges ($PI_{syn,max}$, white dots) and polarized synchrotron emission at 22.8 GHz (red) compared with the eROSITA X-ray emission at 0.6–1.0 keV (green). The large structure close to the east end of the map with no X-ray counterpart is the Fan Region (local emission; Extended Data Fig. 4). The magnetized ridges in the inner Galaxy ($|l| \lesssim 60°$) are spatially correlated with Galactic structures: the ridges associated spatially with the Fermi bubbles appear to emanate from the Central Molecular Zone[8,20,21], while the ridges in the outer region appear to originate in the disk a few kiloparsecs from the Galactic Centre. The ridges show an approximate north–south symmetry. The polarized intensity is enhanced at the edges of the eROSITA bubbles. The eastern edges of these bubbles are parallel to their magnetic field. The western roots of the eROSITA bubbles' edges are limb-brightened in polarized synchrotron emission.

high latitudes. This implies a potential connection between magnetic ridges and the eROSITA bubbles, as the eROSITA bubbles also show a westward tilt.

It is difficult to study the halos of the Milky Way because radiation coming from the Galactic halo is mixed with foreground emission arising in local spiral arms[8,9]. Hence, a key issue for these extended structures is whether they are local objects within the local hot bubble[10], or distant Galactic structures. Thus far, they have mostly been modelled as shells of old supernova remnants in the local hot bubble[7,11]. Figure 2 reveals an anti-correlation between the eROSITA X-ray maps[5] (0.6–1.0 keV) at mid/low Galactic latitudes and the dust column density based on the dust distribution within 500 pc from the Sun[12]. Therefore, the local dust within 500 pc is responsible for the X-ray absorption, implying that the X-ray-emitting eROSITA bubbles are not local and the bulk of the emitting structures must originate from a distance beyond the 500-pc line-of-sight extent of our local arm. This is consistent with the comparison between dust emission and the X-ray data measured by Röntgensatellit (ROSAT) from ref. 13.

https://doi.org/10.1038/s41550-024-02362-0

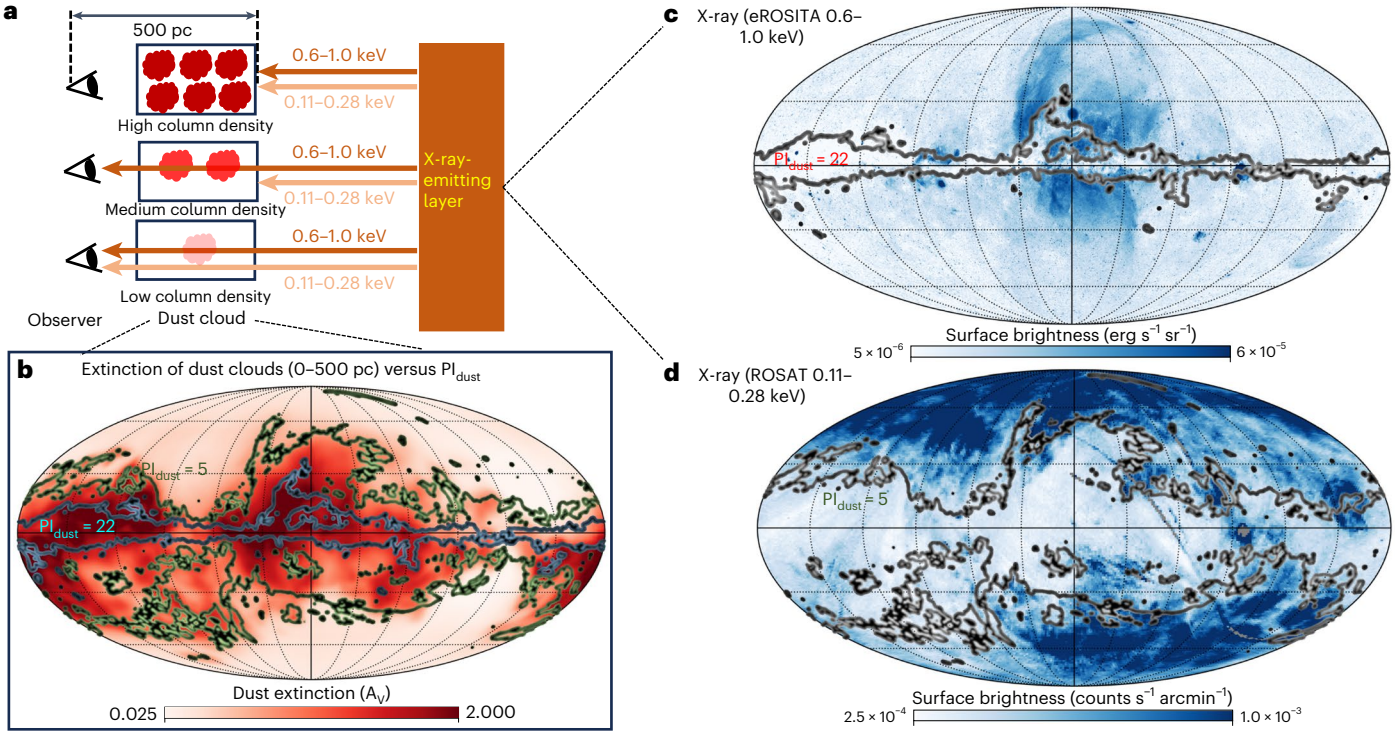

Fig. 2 | Distance measurements to the eROSITA bubbles. a, Schematics illustrating how X-ray absorption depends on the column density of the foreground medium. **b**, The extinction map for the layer at 0–500 pc, as obtained from the 3D dust distribution by using the Gaia-2MASS-Apogee dataset[12] (background image), matches the polarized dust intensity map at 353 GHz from Planck[28]. Contours are two levels of polarized intensity, PI_{dust}. **c**,**d**, An anti-correlation is obvious between high dust column density (**c**, contours, $PI_{dust} = 22$ μK) with high-energy X-ray emission (0.6–1.0 keV), and between low dust column density (**d**, contour, $PI_{dust} = 5$ μK) with low-energy X-ray emission (0.11–0.28 keV).

Extended Data Fig. 2 shows that these magnetic ridges corresponding to the X-ray-emitting outer halo either have no dust counterparts or their directions are not correlated with the magnetic field inferred from the polarized dust emission. Hence, the magnetic ridges are also non-local structures. We estimate our distance from the polarized synchrotron emission of the magnetized ridges in Fig. 3 owing to the Faraday rotation depolarization of the foreground turbulent magnetized medium[14,15]. As demonstrated in Fig. 3a, the depolarization is largest at lower frequencies and decreases at higher latitudes because of a decline with latitude of the magnetic field strength and electron density in the foreground medium, as well as a shorter column through the foreground medium. Using the depolarization expected from the magneto-ionic medium out to different depths, the comparison between Fig. 3b and 3c demonstrates that the observed depolarization is consistent with that produced by the medium out to distances of several kiloparsecs (see Methods and Extended Data Figs. 3 and 4 for details). The polarized magnetic ridges are thus Galactic structures of several kiloparsec scales. This indicates that the bulk of the emission associated with these extended structures (including the North Polar Spur[16]) is beyond several kiloparsecs from us; however, this analysis does not exclude a smaller contribution from some local features.

The fact that synchrotron radiation is enhanced at the edges of the X-ray-emitting halo structures indicates the presence of relativistic electrons. Those electrons can also give rise to gamma-ray emission via inverse Compton (IC) scattering of photons from interstellar radiation and the cosmic microwave background (CMB). We investigate the potential gamma-ray counterparts of the eROSITA bubbles using the Fermi Large Area Telescope (Fermi-LAT) data of the diffuse all-sky gamma-ray intensity from ref. 17. The relative excess of the gamma-ray intensity above the background is presented in Fig. 4a and Extended Data Fig. 5. The horizontal cuts at north and south high Galactic latitudes above and below the Fermi bubbles are shown in Extended Data Fig. 6. We observe that extended structures with γ-ray enhancements show agreement with a large part of the edges of the X-ray-emitting outer halo. The consistency with the eROSITA bubble in the north can be observed in all three gamma-ray maps (with gamma-ray energy $E_\gamma \gtrsim 1$, 10 and 100 GeV) at mid/high latitude ($b > 30°$). The consistency in the south is observed for $E_\gamma \gtrsim 100$ GeV and for $b \gtrsim -60°$ (Extended Data Fig. 6), while no clear structure is observed at the cap of the southern eROSITA bubble.

The eROSITA bubbles contain the Fermi bubbles in projection, but it is extremely difficult to imagine a scenario in which the two Galaxy-scale features are centred at different distances. It is worth noting that the origin of the Fermi bubbles and their potential low-latitude radio counterparts (the so-called radio haze)[18,19] can either be the outflows from the star formation activity of the Central Molecular Zone[20,21] or the past activity of the central supermassive black hole (SMBH) Sgr A*[22,23]. Investigating the origin of the Fermi bubbles is beyond the scope of this work.

Our analysis in this work focusses on the non-thermal emission in the region outside the Fermi bubbles but inside the edges of the eROSITA bubbles (hereafter the 'outer region'). The similarity in the morphology between radio and γ-ray bands implies a common origin of the emission in these bands, and we study the spectral energy distribution (SED). In Fig. 4, two patches within the outer region are selected for further investigation: patch R1 in the north ($20° < l < 40°$, $45° < b < 60°$, where l and b stand for Galactic latitude and longitude) and patch R3 in the south ($20° < l < 40°$, $-45° < b < -30°$). The average flux densities of the two patches outside the eROSITA bubbles at the same Galactic latitudes (patches R2 and R4, respectively) are subtracted from the two selected patches within the outer region to remove fore/background emission from the Galactic halo. The radio data[24–28] from 0.408 to 30 GHz are

https://doi.org/10.1038/s41550-024-02362-0

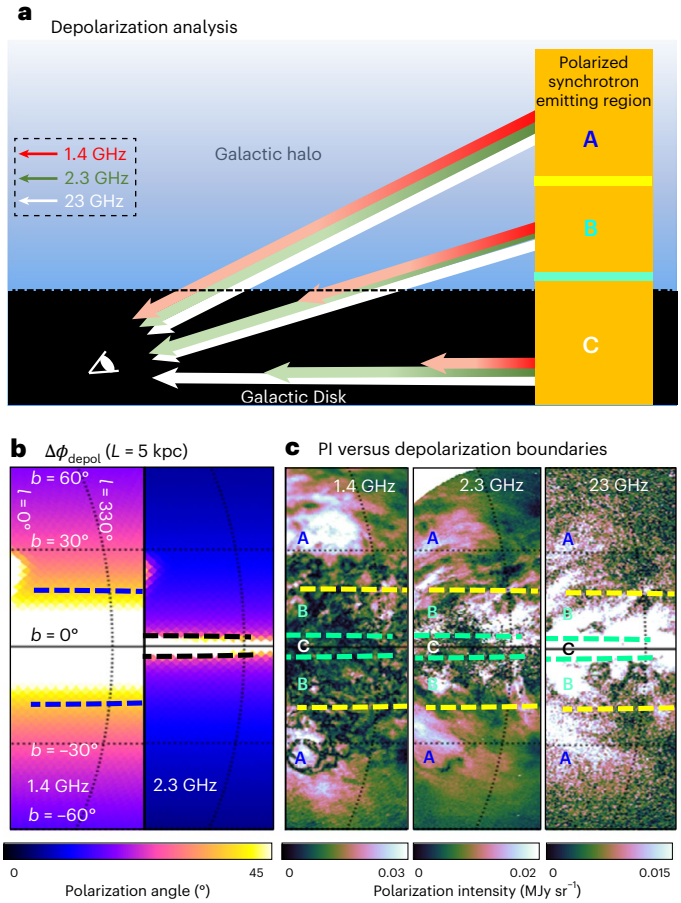

Fig. 3 | Distance measurements for magnetized ridges by Faraday rotation depolarization. a, A schematic showing that, for the polarized synchrotron emission, assuming the Galactic turbulent magnetic field out to 5 kpc, Faraday rotation depolarization is negligible at 22.8 GHz (white, WMAP map). The depolarization occurs up to a few degrees of Galactic latitude at 2.3 GHz (green, S-band Polarization All-Sky Survey, S-PASS), and further extends up to a Galactic latitude of $|b| \approx 20°$ at 1.4 GHz (red, Global Magneto-Ionic Medium Survey) (Extended Data Fig. 3). The structures A–C at different heights hence show different depolarization. **b**, The depolarization screen at 5 kpc for the two lowest frequencies as the latitude at which the depolarization is 0.5 and $\Delta\Phi \approx 40°$. **c**, A comparison of the observed polarized intensity maps. The observations are consistent with an origin of the polarized synchrotron emission at mid/high Galactic latitudes from beyond 5 kpc.

used to characterize the synchrotron emission. The effective area of Fermi-LAT drops quickly with decreasing energy below 1 GeV, leading to poor statistics for diffuse emission in the chosen patches for $E_\gamma \lesssim 0.3$ GeV (ref. 29). Therefore, we use only the data above 0.3 GeV in our study. We fit the spectrum with a single power law in each individual band (radio or gamma ray; Extended Data Fig. 7), and note that the gamma-ray flux density exhibits a softer spectrum compared with the radio flux in the outer region owing to the Klein–Nishina (KN) effect.

Assuming that the same electrons within a given patch are responsible for both the synchrotron emission and IC scattering, we fit the multi-wavelength SED in different patches of the eROSITA bubbles to study the cosmic rays (CRs) and magnetic fields therein (Methods). The best-fit results of the SED fitting are presented in Fig. 4c–e. The SED fitting results demonstrate a north/south symmetry of the outer region of the eROSITA bubbles. The derived electron distributions $N \propto E^{\alpha}$ (E, electron energy; α, spectrum power-law index) have shown consistent, very steep slopes, with $\alpha = -3.40 \pm 0.06$ in the northern patch R1 and -3.38 ± 0.10 in the southern patch R3. The magnetic field directions are largely symmetric about the Galactic Disk, and the average magnetic field strengths are 1.97 ± 0.20 μG in the north and 1.40 ± 0.20 μG in the south. We calculate the plasma beta $\beta \equiv p_{th}/p_B$, where the magnetic pressure is $p_B = B^2/8\pi$ (B is the magnetic field strength) and the thermal pressure is $p_{th} = n_e k_B T$ (n_e is thermal electron density, k_B is the Boltzmann constant and T is the gas temperature). We adopt a temperature of 0.3 keV (refs. 5,30), a halo electron density of 3×10^{-3} cm^{-3} calculated from ref. 31 and the magnetic field strength obtained through our SED fitting. In patch R1, $\beta_{R1} \approx 9$, and in patch R3, $\beta_{R3} \approx 18$.

Plausible origins of the CRs responsible for the non-thermal radiation in the outer region of the eROSITA bubbles include acceleration processes in the inner Fermi bubbles or Galactic outflows from the disk. As a comparison, we perform an SED fitting for the south-eastern edge of the Fermi bubbles in Fig. 4e and find an electron energy index of $-3.00^{+0.3}_{-0.13}$ for patch R5. This electron index is harder than that in patch R3 of the outer region at the same latitude. We compare the synchrotron flux densities for the outer patch R3 and the inner patch R5 after foreground subtraction, yielding $F_{\nu,R3} = 0.0523 \pm 0.0078$ MJy sr^{-1} and $F_{\nu,R5} = 0.0140 \pm 0.0099$ MJy sr^{-1} for 0.408 GHz, $F_{\nu,R3} = 0.0082 \pm 0.052$ MJy sr^{-1} and $F_{\nu,R5} = 0.0118 \pm 0.0059$ MJy sr^{-1} for 1.4 GHz, $F_{\nu,R3} = (5.9 \pm 4.6) \times 10^{-4}$ MJy sr^{-1} and $F_{\nu,R5} = (3.4 \pm 6.7) \times 10^{-4}$ MJy sr^{-1} for 23 GHz, and $F_{\nu,R3} = (3.3 \pm 1.3) \times 10^{-4}$ MJy sr^{-1} and $F_{\nu,R5} = (1.5 \pm 1.4) \times 10^{-4}$ MJy sr^{-1} for 30 GHz. The synchrotron flux densities in the outer region are equivalent to or higher compared with the foreground-subtracted values inside the Fermi bubbles at a similar Galactic height. Therefore, diffusion from the Fermi bubbles cannot be the primary process for injecting the relativistic electrons into the outer region. In addition, the magnetic field is parallel to the shell of the bubbles and the diffusion from the Fermi bubbles into the outer halo requires cross-field transport of relativistic electrons, which is very inefficient.

Figure 5 shows that the magnetic ridges of the outer region connect to the areas having high star-formation rates in the disk. These areas correspond to the star-forming ring located 3–5 kpc from the Galactic Center (GC), at the end of the Galactic Bar. The magnetized ridges related to the Fermi bubbles, on the other hand, appear to originate from the few-hundred-parsec Central Molecular Zone and to wrap around the surface of the Fermi bubbles, which is consistent with previous works[8,22]. This distinction is also consistent with the conclusion above that there are different origins of the relativistic electrons in the Fermi bubbles and those in the outer region (the region between the outer boundaries of the Fermi and eROSITA bubbles). In search of the sources of relativistic electrons, we show in Extended Data Fig. 8 a polar view of the specific star-formation rate distribution in the Milky Way, as measured by Herschel[32], displaying several clumps in the 3–5-kpc star-forming ring with rates $\Sigma_{SFR} \gtrsim 0.02\ M_\odot\ yr^{-1}\ kpc^{-2}$. This distribution aligns with the footprints of the magnetized ridges, which gives us a clue to the origin of the relativistic electrons in the outer region. The collective effect of merging supernova explosions can generate a Galactic wind by expelling material at speeds ranging from 100 to 1,000 km s^{-1} out of the Galactic Disk[33–36]. Consequently, a wind termination shock is anticipated at the high-altitude extent of the wind, where particles are accelerated and heated. Hence, the primary source of CRs responsible for the outer region is likely to be Galactic outflows from the 3–5-kpc star-forming ring (hereafter 'outer outflows'). The radio/gamma flux densities in the outer outflows can be effectively modelled with electrons having energies higher than 2 GeV, following a single power-law distribution. This supports the hypothesis of a shared origin for the multi-wavelength radiations. The electron index of $\alpha \approx -3.4$ observed in the outer outflows is too soft with respect to the expectation from strong shock acceleration (the classical value for the index in a strong shock is $\alpha = -2$)[37,38]. Instead, the observed soft spectrum arises from a substantial cooling above 2 GeV within the investigated patches. This indicates that the dynamic time scale of the outer outflows is longer than the cooling time scale of the relativistic electrons, 10^8 yr (Methods). In this scenario, the thermal X-ray

https://doi.org/10.1038/s41550-024-02362-0

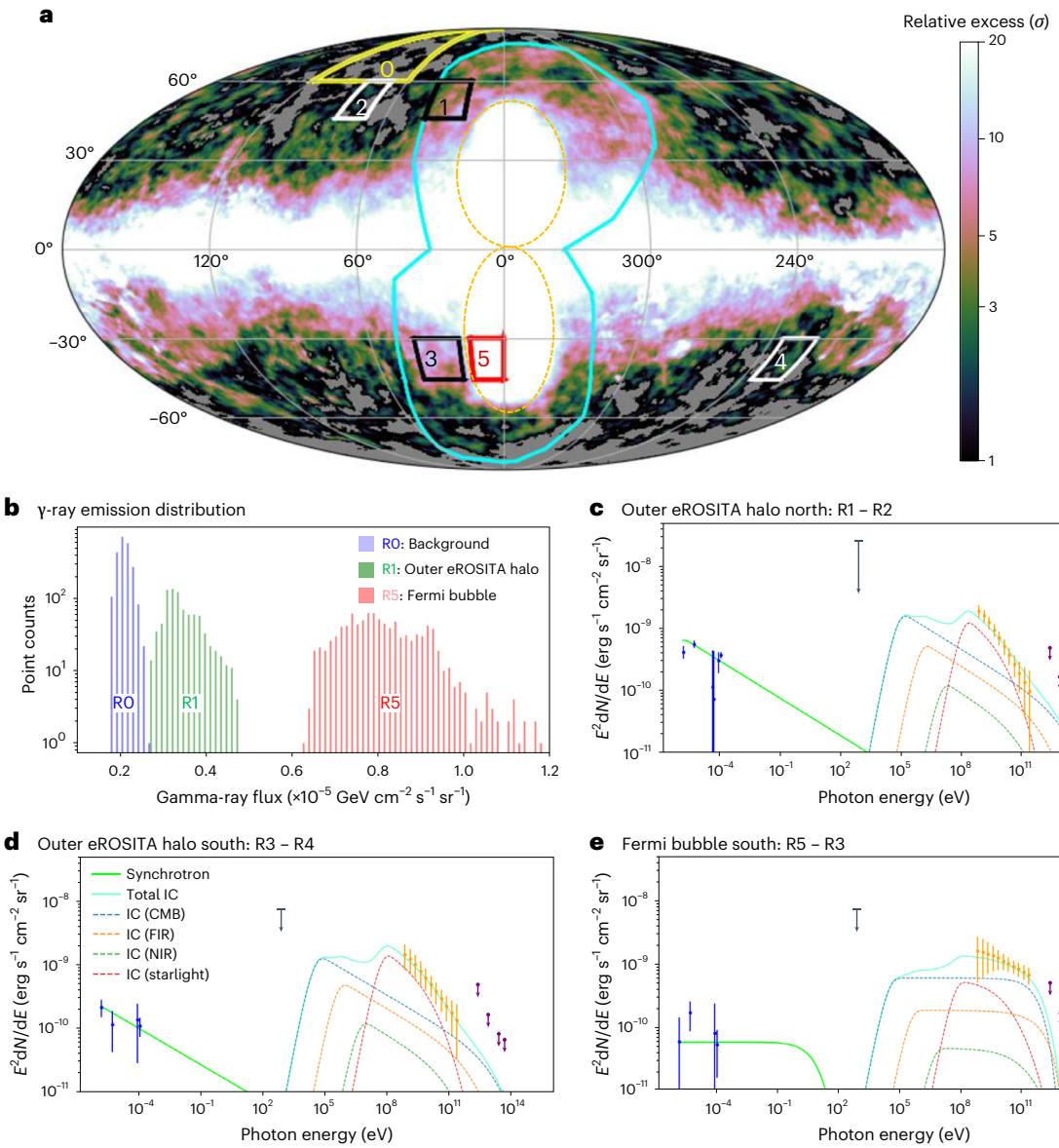

Fig. 4 | Radio/γ-ray analysis and SED. a, Intensity map (defined in Methods) of the Fermi all-sky diffuse map at $E_\gamma \geq 100$ GeV, expressed in units of the noise level from the reference background (patch R0 in the north-eastern high galactic latitude sector; see 'Comparison with diffuse gamma-ray radiation' section in Methods for details). Patches R1–R5 are used for the SED study. The two lines are the edges of the eROSITA (solid) and Fermi (dashed) bubbles. **b**, The distribution of the pixel counts for the gamma-ray fluxes in the background (R0), the outer region of the eROSITA bubbles (R1) and the Fermi Bubble (R5). The three distributions are well separated. **c**–**e**, The SED best fit of leptonic radiation in the outer region north (R1 − R2) with electron energy index −3.40 ± 0.06 and magnetic field 1.97 ± 0.20 μG (**c**), in the outer region south (R3 − R4) with electron index −3.38 ± 0.10 and magnetic field 1.40 ± 0.20 μG (**d**) and in the south-eastern cap of the Fermi bubble (R5 − R3) with electron index $-3.00^{+0.30}_{-0.13}$ and magnetic field $1.0^{+0.5}_{-0.4}$ μG (**e**). The black vertical arrows are the upper limit from the X-ray surface brightness, and the violet vertical arrows are the upper limit from the High Altitude Water Cherenkov (HAWC) sensitivity in TeV gamma-ray band. The error bars on the gamma-ray data points are based on the statistical uncertainties (see 'Data and errors for SED' section in Methods for details). The reference frequencies are listed in Supplementary Table 2. The error bars on the radio fluxes are calculated on the basis of the flux density calibration accuracy and beam sensitivity of the corresponding surveys, as defined in the Supplementary Information. The fitting results for the electron distribution indices for the outer regions are consistent, but the Fermi bubble has a harder electron energy distribution index. The detailed results are summarized in the Supplementary Information.

emission of the eROSITA bubbles comes from the shock-heated plasma. Applying the Rankine–Hugoniot relation, we find that the wind velocity is approximately $v_w \approx 400$ km s^{-1} (Methods), falling within the anticipated range for galactic winds driven by collective supernova explosions. Our calculations indicate that sustaining the outer outflows up to 10 kpc height requires less than 21% of the energy released from supernova explosions in the 3–5-kpc star-forming ring and the mass loss rate from the star-forming ring would be 0.3–1.3 $M_\odot$ yr^{-1} (see calculations in 'Outer outflow modelling' section in Methods and Extended Data Table 1). Our results are consistent with prior hydrodynamical simulations[39] focussing on the thermal emission from the eROSITA bubbles.

We present a detailed three-dimensional (3D) picture for the eROSITA bubbles in Fig. 5c, where the outflows form a 'bouquet' shape in the Galactic halo. Our geometric check in the Supplementary Information shows that a 'bouquet' outer halo can be projected into a bubble shape (Methods and Extended Data Fig. 9). In our model, magnetic ridges appear as coherent structures emerging from the active star-forming regions in the Galactic Disk. Previous research[8,40,41]

https://doi.org/10.1038/s41550-024-02362-0

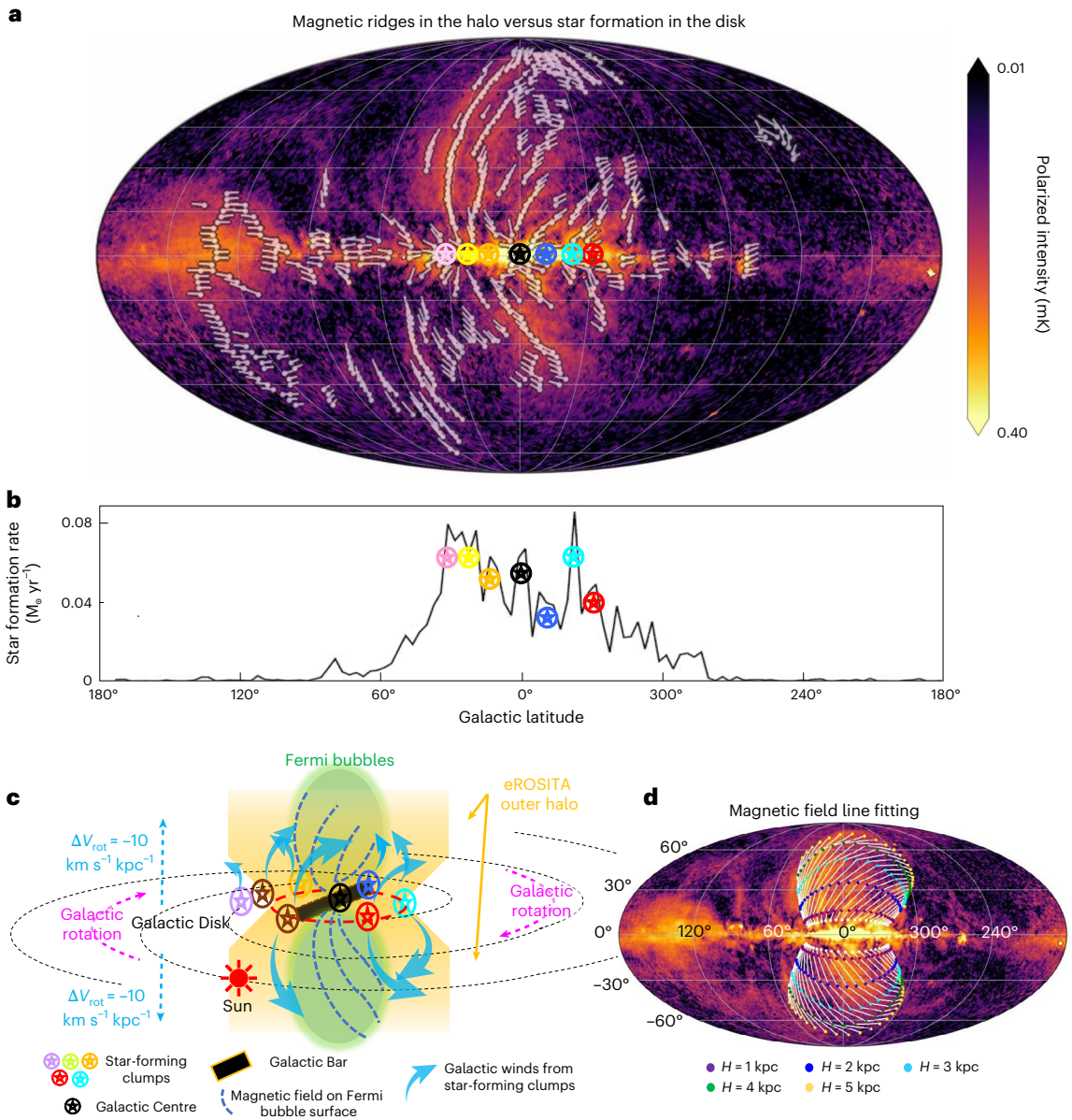

Fig. 5 | Energy sources of the Galactic outflows. a, The polarized intensity map at 22.8 GHz by WMAP with the magnetic ridges (white) overlaid. **b**, The star formation rate on the Galactic plane as measured by ref. 32, where footpoints of the magnetic ridges correspond to the marked clumps with high values. A north polar view of the active star-forming clumps is shown in Extended Data Fig. 8. **c**, The proposed scenario for the observed multi-wavelength Milky Way outflows. The 3–5-kpc star-forming ring powers the outer outflows, showing a 'bouquet' morphology. We assume the presence of a central outflow that generates the Fermi bubbles, as discussed in previous works[20,22]. We note that some magnetized ridges appear to be wrapped around the Fermi bubbles. The outflows show a lag as the plasma is transported to higher Galactic latitudes because of the decrease of rotational speed at higher heights from the plane (ΔV_{rot}). **d**, Modelling of the field line flow wrapping around the surface of the outer outflows. An angular lag of 4.5° $\frac{H}{\mathrm{kpc}}$ with increasing height H is used. The east-to-west tilted orientation of the magnetic ridges can be reproduced by such lagging. The resulting magnetic field is parallel to the surface of the bubbles, providing confinement to the CRs.

revealed that the Galactic halo medium rotates clockwise as seen from Galactic north, similar to the the Galactic Disk, and that the azimuthal angular speed decreases with height above the disk. This is a natural consequence of the conservation of angular momentum as the outflowing winds expand into the halo. Indeed, external spiral galaxies show a similar behaviour and have been found to have a lag in the halo, with a reduction of the gas rotational speed on the order of 10 km s^{-1} $\frac{H}{\mathrm{kpc}}$ (refs. 42,43), where H is the height above the Galactic plane. Figure 5d shows that the angular lag of outflowing gas with increasing height from the Galactic plane is compatible with the general orientation of the magnetic field, aligned with the magnetic ridges showing a global westwards-oriented tilt from the Galactic Disk into the halo. Recent simulations[44] of the magnetic halo of a galaxy found that ordered magnetic fields are associated with free gas winds in galactic outflows, whereas more turbulent fields appear in the shocked region. Thus, these magnetic ridges in the Galactic halo probably trace the outflowing winds. This is consistent with what was previously found for the magnetic ridges wrapping the Fermi bubbles[8], thus suggesting similar gas dynamics for the inner and outer outflows.

Our data analysis and modelling lead us to propose that the 3–5-kpc star-forming ring powers the eROSITA Galactic outflows, which result in both thermal and non-thermal large-scale emission. As shown

in Fig. 5a, magnetic ridges are connected to the active star-forming regions on the Galactic Disk rather than the GC, which supports our proposed scenario. Earlier investigations have also discussed the possibility that the thermal emission from the outer region results from the Fermi bubbles' expansion because of either previous active galactic nucleus (AGN) activities[45–48] of the SMBH Sgr A* or outflows from starburst regions at the GC[49]. Whether these GC outflow scenarios can reproduce magnetic structures such as those in Fig. 5a is unclear, and dedicated simulations are needed to answer this question. With our findings, future research focussing on the circumgalactic medium of the Milky Way should take the magnetic halo and the non-thermal fluxes in the corresponding regions into account while analysing the X-ray halo. In addition, future studies of the Milky Way's outflows should consider the 3–5-kpc star-forming ring as another potential energy source other than the SMBH and the starburst activities at the GC.

Our results indicate a connection between the X-ray-emitting and magnetized Galactic halos and offer insights into the origin of these halos in other galaxies. We have shown that galactic-scale star-forming activities play a strong role in the formation of magnetically organized structures within galactic halos. Notably, observations of edge-on galaxies have revealed a distinctive X-shaped magnetic halo at radio frequencies, featuring kiloparsec-scale anisotropic magnetic ridges emerging from the galaxies' inner region[3]. Such features can be attributed to galactic outflows launched from active star-forming regions, which can regulate the gas ecosystem of galaxies and have a fundamental impact on galaxy evolution.

Methods

Distance measurements through multi-wavelength observations

A key issue that we want to answer is whether those gigantic structures projected in the sky are within the Local Arm or stemming out of the Galactic Disk at much further distance from us. In this section, we present our distance estimates through multi-wavelength comparison using X-ray versus dust observation, dust versus synchrotron polarization and Faraday rotation depolarization analysis based on multi-frequency synchrotron data.

X-ray versus dust observations. We estimate the distance to the X-ray-emitting eROSITA bubbles in Fig. 2. The X-ray photons emitted by hot plasma can be absorbed by foreground medium. Figure 2b shows that the polarized dust intensity from the Planck survey is originated mainly from the local medium. We take the measurements from ref. 12 and integrate the extinction for distances lower than 500 pc around the Sun, as obtained from the 3D dust distribution by the Gaia-2MASS-Apogee dataset. Figure 2c shows that an anti-correlation is observed between the eROSITA bubbles (0.6–1.0 keV) and the contour of polarized intensity from the dust at $PI_{dust} = 22$ μK. On the other hand, Fig. 2d reports the anti-correlation between the softer X-ray emission from the Röntgensatellit[50] (0.11–0.28 keV) and the contour of a lower polarized intensity from the dust ($PI_{dust} = 5$ μK). The X-ray absorber for softer X-ray emission has extended to a higher Galactic latitude. This is consistent with the picture that the bulk of the X-ray-emitting structure is behind the dust within 500 pc, as illustrated in Fig. 2a. Therefore, we conclude that the eROSITA bubbles stand behind the dust emission within 500 pc from the Sun, beyond the Local Arm. Hence, they should extend above and below the Galactic Disk.

Dust versus synchrotron polarization. We obtain the magnetic ridges by performing same-latitude cuts across the all-sky polarized synchrotron emission map (PI_{syn}) from the WMAP K band[6] to find the local maximum points ($PI_{syn,max}$) along each cut. The points with $PI_{syn,max} > 0.04$ K are preserved in Fig. 1, and the corresponding magnetic field directions are overlaid. Several coherent magnetic structures extending more than 15° are found, and we define them as magnetic ridges. Figure 2b demonstrates that the polarized dust intensity from the Planck survey are originated mainly from the thermal dust within 500 pc from us. This agrees with the previous simulations[51] that the dust emission observed at 353 GHz agrees with the radiation of dust from the Local Bubble, which is within 200 pc from the Sun[52,53]. Extended Data Fig. 2 presents a comparison between the polarization angles of dust (353 GHz) and the magnetic field inferred from the synchrotron polarized emission. The polarization angle of dust emission at millimetre wavelengths is perpendicular to the magnetic field. As shown in Extended Data Fig. 2b, the known local structures, the Fan Region and most of the Galactic plane ($|b| < 5°$) apply to the polarized E-vector of the dust emission perpendicular to the magnetic field. There is no uniform correlation between the magnetic field and the polarized dust emission in the Serpens–Aquila Rift. Furthermore, most of the magnetic ridges corresponding to the outer region of the eROSITA bubbles and the southern Fermi bubbles have no dust counterparts. Hence, these ridges are Galactic structures that are not contaminated with other components along the line of sight. Because the polarized synchrotron emission also does not have the distance information for the emitting layer, we introduce the Faraday rotation depolarization analysis in the next section to measure the distances to those magnetic ridges.

Faraday rotation depolarization analysis. The depolarization is the ratio between the polarization fraction at a frequency and that at a reference frequency, assumed not depolarized. The polarized intensity and polarization angles of the magnetic ridges show wavelength-dependent depolarization. On the basis of the derivations from refs. 14,15,54, the wavelength-dependent Faraday depolarization for a synchrotron-emitting and Faraday-rotating turbulent magneto-ionic plasma is

$$f_{\rm depol} = \frac{1-\exp(-S)}{S}, \tag{1}$$

where $S \equiv 2\sigma_{\rm RM}^2\lambda^4$, where λ is the wavelength of the signal. In our calculations, we pick the 22.8 GHz value of the WMAP[55] data as the reference frequency, at which the Faraday rotation depolarization can be assumed negligible. The Faraday rotation measure (RM) dispersion $\sigma_{\rm RM}$ is

$$\sigma_{\rm RM} = 0.81\,\sigma_{\rm B\parallel}\,n_{\rm e}\,d\,N_{\parallel}^{1/2}, \tag{2}$$

where $n_{\rm e}$ (cm^{-3}) is the electron number density of the plasma, $\sigma_{\rm B\parallel}$ (μG) is the component along the line of sight of the isotropic, turbulent magnetic field and $N_{\parallel}$ is the number of random-walk cells of length d (pc) along the line of sight. The latter is defined as $N_{\parallel} \equiv Lf/d$, where L (pc) is the distance from us and $f \equiv \langle n_{\rm e}\rangle^2/\langle n_{\rm e}^2\rangle$ is the electron volume filling factor. The RM dispersion can thus be written as[56]

$$\sigma_{\rm RM}^2 = \left(0.81\sigma_{\rm B\parallel}\right)^2 L\,d\,\langle n_{\rm e}^2\rangle. \tag{3}$$

We adopt $d = 100$ pc following refs. 54,57,58. We use the electron density model by ref. 59. We assume a distance of the Sun from the Galactic Centre of $D_\odot = 8.5$ kpc. Given a position on the line of sight with Galactic coordinates (l, b) and a distance L from the Sun, the position in the Galaxy can be expressed as

$$\begin{aligned} r &= \sqrt{D_\odot^2 + L^2\cos^2(b) - 2D_\odot L\cos(b)\cos(l)},\\ z &= L\sin(b), \end{aligned} \tag{4}$$

where r is the separation from the Galactic Centre on the Galactic plane and z is the height from the plane. Along each line of sight, we

perform the integration with a discrete step $\delta L = 5$ pc, which yields an RM dispersion of

$$\sigma^2_{\rm RM} = \int_L^O \left(0.81 B_\parallel(l,b,L)\right)^2 d\, n_e^2(l,b,L)\delta\mathbf{L} = \int_L^O \left(0.81 B^{\rm JF12}_\parallel(l,b,L)\right)^2 d\, n_e^2(l,b,L)\delta\mathbf{L}. \quad (5)$$

We take the Jansson&Farrar12 (JF12) magnetic field model[60] of the Milky Way, modified to fit the Planck results[61]. Here, $B^{\rm JF12}_\parallel = B^{\rm JF12}_{\rm regular,\parallel} + 1/\sqrt{3} B^{\rm JF12}_{\rm turb}$ is the magnetic field strength adopted from refs. 60,61, $B^{\rm JF12}_{\rm regular,\parallel}$ is the line-of-sight projection of the regular magnetic component and $B^{\rm JF12}_{\rm turb}$ is the strength of the turbulent component. In addition, the wavelength-dependent dispersion caused by the foreground medium with $\sigma_{\rm RM}$ is

$$\Delta\Phi = \sigma_{\rm RM}\lambda^2. \quad (6)$$

The results from these equations are shown in Fig. 3. Extended Data Fig. 3 demonstrates the Faraday rotation depolarization for synchrotron-emitting structures at different distances. We estimate the depolarization from the observations at three different frequencies (22.8, 2.3 and 1.4 GHz using data from WMAP[6,55], the S-band Polarization All-Sky Survey[8,62] (S-PASS) and the Dominion Radio Astrophysical Observatory (DRAO)/Villa-Elisa surveys[25,63], respectively). The depolarization gets smaller moving to high latitudes and higher frequencies. The depolarization screen generated by the magneto-ionic medium out to 5 kpc is reported in Fig. 3. Our calculations show that the depolarization depends on the frequency and the latitude that determines how much of the disk the polarized radiation goes through. Specifically, as shown in Fig. 3a, for zone A (high latitudes, $|b| \gtrsim 20°$), both 1.4 and 2.3 GHz can be observed; for zone B (mid latitudes $5° \lesssim |b| \lesssim 20°$), 1.4 GHz is depolarized while 2.3 GHz is observable; for zone C (low latitudes, $|b| \lesssim 5°$) both 1.4 and 2.3 GHz are depolarized. Negligible depolarization occurs at 22.8 GHz at any latitudes, and the magnetic coherence is preserved from the Galactic Disk up to the Galactic Poles. Figure 3c shows the polarized emission observed at 1.4 GHz (DRAO/Villa-Elisa)[25,63], 2.3 GHz (S-PASS)[8,62] and 22.8 GHz (WMAP)[6,55]. The image shows that our calculations of the depolarization broadly match the regions of high depolarization. Extended Data Fig. 4 presents a detailed analysis for the comparison between all-sky polarized synchrotron-emitting structures at 1.4 and 22.8 GHz, and the depolarization screen at the distance $L = 5$ kpc. In the eastern sky of Extended Data Fig. 4b, the regions with high polarization intensity at 1.4 GHz are observed at low Galactic latitudes (that is, the Fan Region and Loop III). Different from the central magnetic ridges, these regions can be interpreted as local, or at a distance closer than some 1 kpc. This is consistent with previous measurements at 150 MHz (ref. 64). Instead, the Galactic magnetized ridges coincident to the eROSITA bubbles are clearly depolarized at 1.4 GHz at low and mid Galactic latitudes, consistently with the prediction of a depolarization screen at a distance of at least 5 kpc. The frequency-sensitive depolarization does not affect the local structures.

Consistency of the X-ray eROSITA bubbles' edges with emission at other wavelengths

In this section, we discuss the comparison between the edges of the X-ray-emitting eROSITA bubbles and the enhancements at other wavelengths. While the radiations in the radio and gamma-ray bands result from different radiation processes than the X-ray, large-scale enhancements from these bands are observed to be coincident with the edges of the eROSITA bubbles by an offset of only a few degrees.

Comparison with synchrotron emission. We compare the magnetized ridges, as we defined them using synchrotron polarization data from WMAP[6,55], with the X-ray surface brightness at 0.6–1.0 keV in Extended Data Fig. 1. The polarized intensity peaks ($\rm PI_{syn,max}$) are observed close to the edges of the eROSITA bubbles with an offset of only a few degrees. Therefore, these Galactic magnetic ridges are enhanced close to the edges of the eROSITA bubbles, with the only exception of the south-west bubble's edge. The enhancements of $\rm PI_{syn}$ at all four roots of the eROSITA bubbles suggests that the eROSITA bubbles are limb-brightened in synchrotron polarized emission, similarly to the roots of the Fermi bubbles[8,22]. The magnetic field directions are parallel to the eastern edges of the eROSITA bubbles in both the north and the south. Instead, there is no such alignment in the west. A possible explanation is given by the modelling presented in the main text and Fig. 5d. The points at the same height ($H = 1$–5 kpc) on the eROSITA bubbles' surface are projected on the polarized synchrotron intensity map. An anticlockwise lag of 4.5° is introduced between points differing in height by $\Delta H = 1$ kpc, which is a natural outcome of the conservation of angular momentum as the outflowing winds expand into the halo. The tracks of the gas in Galactic outflows have a global east-to-west tilt from the Galactic Disk towards higher latitude, and they are consistent with the observed magnetic ridges.

Comparison with diffuse gamma-ray radiation. In our γ-ray intensity map, we calculate the relative excess of the γ-ray flux along different lines of sight, comparing with the standard deviation of the selected background area located at high Galactic latitude towards the north-east (Fig. 4, patch R0). The relative excess is defined by $\sigma \equiv (I_{\rm f} - \bar{I}_{\rm f0})/{\rm std}(I_{\rm f0})$, where $I_{\rm f}$ is the flux at a given line of sight, $\bar{I}_{\rm f0}$ and ${\rm std}(I_{\rm f0})$ are the average value and standard deviation of the background patch. The results are presented in Fig. 4a and Extended Data Fig. 5. The northern edges of the eROSITA bubble are consistent with $\sigma \gtrsim 5$ for all three energy bands. For the Galactic south, the diffuse gamma-ray emission for $E_\gamma \gtrsim 100$ GeV has shown an enhancement at the edges of the southern eROSITA Bubble up to $l \approx -60°$ in latitude. But it is less clear for the other two energy bands. The more detailed comparison between X-ray and γ-ray at $E_\gamma \gtrsim 100$ GeV for eROSITA bubbles is performed in Extended Data Fig. 6. We perform cuts in high Galactic latitudes in the north ($b = +70°$ and $+65°$) and south ($b = -60°$) to avoid the potential influence by the emission from the foreground Galactic Disk or the Fermi bubbles. In the northern cuts, both X-ray and γ-ray radiations have shown central enhancements ($-70° \lesssim l \lesssim 40°$) beyond the background within the edges of the eROSITA bubbles with a clear 'plateau' shape. In addition, the edges of the enhancements are in agreement with an offset of only a few degrees. In the southern cut, the central enhancements are observed for both X-ray and γ-ray bands, but they are less evident as compared with the cuts in the Galactic north. Below $b = -60°$, there is no clear edge of γ-ray-emitting structures.

We intend to compare the correlation between different extended structures at large scales (several tens of degrees). Indeed, the edges of the eROSITA bubbles have shown a consistency with enhancements of polarized synchrotron intensity/gamma-ray intensity within a separation of a few degrees. However, at smaller scales down to a few degrees, the emission could be subject to the local physical conditions, which may vary from place to place. In particular, X-ray emission comes from the thermal electrons, the radio continuum comes from synchrotron radiation of non-thermal electrons in the magnetic field, and gamma-ray photons come from IC scattering of non-thermal electrons. Their radiation efficiencies do not rely on the same physical quantities. Therefore, we do not expect a perfect correlation down to a few degrees.

SED analysis

In this section, we provide details for our SED analysis, including data and errors, fitting for the photons of IC, Markov chain Monte Carlo (MCMC) fitting and fitting results.

Data and errors for SED. The spectral energy is computed as

$$E^2 d^4N/(\mathrm{d}E\,\mathrm{d}A\,\mathrm{d}\Omega\,\mathrm{d}t), \tag{7}$$

which we will introduce for different bands of data we use below.

For γ-ray, equation (7) is the energy of the photons received at the receiver (area A) at a given band width (log-spaced) per solid angle per time (using the notation $E^2\mathrm{d}N/\mathrm{d}E$ for simplicity).

For radio data, the spectral flux density ($\mathcal{F}(\nu)$) is the quantity that describes the rate at which energy is transferred by electromagnetic radiation through a surface, per unit surface area and per unit frequency. $\mathcal{F}(\nu) = \frac{\partial F}{\partial \nu}$, where F is the flux density. The SED quantifies the energy emitted by a radiation source in the log energy band, hence equation (7) is (in the unit of erg s^{-1} cm^{-2} sr^{-1})

$$\begin{aligned}\nu\mathcal{F}(\nu) &= \nu\frac{\partial F}{\partial \nu} = \frac{\partial F}{\partial(\log(\nu))}\\ &= \frac{S[\mathrm{MJy\,sr^{-1}}]}{10^{17}\,\mathrm{MJy}/[\mathrm{erg\,s^{-1}\,cm^{-2}\,Hz^{-1}}]} \times \nu[\mathrm{Hz}].\end{aligned} \tag{8}$$

For the γ-ray flux density, we use the data of diffuse emission from Fermi-LAT. The High Altitude Water Cherenkov (HAWC) sensitivity is used as upper limits for $E_\gamma \gtrsim 1$ TeV as the bubbles are not observed by HAWC[65]. We use two methodologies to extract the diffuse gamma-ray emission of the given patches:

(1) We use the diffuse radiation after the point sources subtraction from Platz+[17] using a Bayesian analysis on the 12-year Fermi data (hereafter Platz+). Platz+ separated the data in the range $0.316\ \mathrm{GeV} \lesssim E_\gamma \lesssim 316\ \mathrm{GeV}$ into 11 energy bins. To compute data uncertainties, we consider (1a) the standard deviation of the flux intensity among all pixels in the patch ($n_{\mathrm{st}} = \mathrm{std}(I_{\mathrm{R}})$) and (1b) the Poisson noise of the observed photons ($n_{\mathrm{Pois}} = \frac{\sqrt{N}}{N}\bar{I}_{\mathrm{R}}$, where N is the total number of photons and $\bar{I}_{\mathrm{R}}$ is the average flux intensity in the patch). Hence, the total error of the patch is defined by $\mathrm{err}_{\mathrm{R}} = \sqrt{n_{\mathrm{st}}^2 + n_{\mathrm{Pois}}^2}$. We then use the normal error propagation rules to compute the uncertainty of the gamma-ray maps. Taking patch R1 subtracted by patch R2 as an example, then,

$$\begin{aligned}&\text{Signal}: I_{\mathrm{signal}} = I_{\mathrm{R1}} - I_{\mathrm{R2}}\\ &\text{Noise}: s_{\mathrm{noise}} = \sqrt{(\mathrm{err}_{\mathrm{R1}})^2 + (\mathrm{err}_{\mathrm{R2}})^2}\end{aligned} \tag{9}$$

where $\mathrm{err}_{\mathrm{R1}}$ and $\mathrm{err}_{\mathrm{R2}}$ are the total errors in patch R1 and patch R2.

(2) Complementarily, we take the diffuse γ-ray data of the same patches from the 14-year Fermi-LAT data (hereafter Fermi14yr). Fermi14yr uses the most recent Fermi data and the 14-year source catalogue 4FGL-DR3[66]. Fermi14yr separates the data in the range $0.1\ \mathrm{GeV} \lesssim E_\gamma \lesssim 500\ \mathrm{GeV}$ into 14 energy bins (the low-energy bins with poor statistics due to a small effective area will not be used for further calculations). We mask the influence from the point sources within a radius of 14° from the boundaries and find the best fit for the diffuse emission through Fermipy[67]. The outcome indices ($\mathrm{d}N/\mathrm{d}E \propto E_\gamma^{\beta_{\mathrm{F14}}}$) for the emission from the five patches by a power-law fitting are (listing here only the statistical errors) −2.180 ± 0.002 for patch R1, −2.235 ± 0.003 for patch R2, −2.205 ± 0.002 for patch R3, −2.167 ± 0.002 for patch R4 and −2.092 ± 0.002 for patch R5. We can see that these fitting indices are rather similar to each other. Therefore, it is necessary to exclude the Galactic foreground influences in our analyses.

To perform fore/background subtraction in our fitting, we remove the average flux outside the bubbles' edge at the same latitude. In the south-eastern sky ($b > 30°$, $60 \lesssim l \lesssim 150°$), there are several known local structures that might influence the estimate of the total flux (Extended Data Figs. 2a and 4). Therefore, we select patch R4 in the southwestern sky to represent the foreground. As demonstrated in Fig. 4a, we choose the patches in the mid-latitude: R1 and R3 for the northern/southern outer region of the eROSITA bubbles, R5 for the southern Fermi bubble cap (the northern Fermi bubble is not selected because it is overlapped with the Serpens–Aquila Rift; Extended Data Fig. 2b). To exclude the influence of the emission of the fore/background, we subtract the emission at the same Galactic latitude outside the considered patches (that is, patch R1 − patch R2, patch R3 − patch R4 and patch R5 − patch R3). We plot the flux density of 0.6–1.0 keV at the corresponding patches from ref. 5 in the SED for reference.

Fitting of the photon field for IC. Based on our analysis, the patches that we study would be only a few kiloparsecs away from the Galactic Disk, hence the seed photons in IC radiations of the SED fitting are mainly from the interstellar radiation field plus the CMB. We neglect the slight anisotropy in the starlight radiation field and only consider the fitting of radiation energy density based on the radiation model proposed in ref. 68 and simplify the seed photon field by fitting the radiation spectrum with four blackbody radiation fields: 'CMB' (at 2.725 K), 'FIR' (far-infrared), 'NIR' (near-infrared) and 'starlight' (scattered starlight from the spiral arms of the Galaxy). We present the four blackbody modellings in Supplementary Fig. 1–3a and summarize the results in Supplementary Table 1a.

MCMC fitting for SED. We use the package 'naima'[69] to model the multi-wavelength results. We choose to see if the multi-wavelength emission fits purely leptonic processes (synchrotron + IC). We assume that the synchrotron emission and IC are from the same electron distributions of the same patches. The synchrotron emission spectrum of the 'naima' package is calculated from the magnetic field strength and the electron distribution based on ref. 70. The IC emission spectrum of the 'naima' package is calculated from the seed photon fields and the electron distribution based on ref. 71.

We presume the electron distribution to be in a power law following the equation defined in 'naima'

$$f(E_{\mathrm{e}}) = A_{\mathrm{e}}\left(\frac{E_{\mathrm{e}}}{1\,\mathrm{TeV}}\right)^{\alpha}, \tag{10}$$

where A_{e} (eV^{-1}) is the amplitude of the electron spectrum, α is the electron index and E_{e} is the electron index.

The non-detection of the bubbles from the HAWC survey provides the upper limit in our SED fitting in $E_\gamma \gtrsim 1$ TeV bands. As a result, the SED data cannot be fitted with a single power-law distribution of electrons. We also test the electron distribution with an exponential cut-off at the high-energy end of the electron spectrum following the equation defined in 'naima'

$$f(E_{\mathrm{e}}) = A_e\left(\frac{E_e}{1\mathrm{TeV}}\right)^{\alpha}\exp\left(-\left(\frac{E_{\mathrm{e}}}{E_{\mathrm{cutoff}}}\right)^{\beta_{\mathrm{e}}}\right), \tag{11}$$

where we take $\beta_{\mathrm{e}} = 2$ as the cut-off power index based on ref. 72.

In our fitting, linear priors are used for all the parameters and the first 500 steps are discarded as the burn-in phase. We run 5×10^3 steps to get the best fit and errors of the amplitude A_{e}, the index α and the magnetic field strength B. The MCMC processes and corner maps are presented in the Supplementary Information, showing that the multi-wavelength data dispersion is within 2σ to the best fit. The fit results are summarized in Supplementary Table 1b.

Fitting results. We first show the power-law fit for the fluxes of individual energy bands in Extended Data Fig. 7: the radio flux ($F_\nu \propto E_\gamma^{\alpha_r}$), and the gamma-ray flux ($E\mathrm{d}N/\mathrm{d}E \propto E_\gamma^{\alpha_{\mathrm{Pl}}}$ for Platz+[17] and $E\mathrm{d}N/\mathrm{d}E \propto E_\gamma^{\alpha_{\mathrm{F14}}}$ for the Fermi 14-year diffuse map[66]).

The gamma-ray spectral indices obtained from the two tested methods have small differences ($\Delta\alpha_\gamma \lesssim 0.1$, for example, for the north-eastern outer halo, $\alpha_{\rm PL} = -1.499 \pm 0.004$ and $\alpha_{\rm F14} = -1.422 \pm 0.008$). They are consistent with each other considering the systematic uncertainties of Fermi-LAT[73]. For reference, the power-law index obtained in the south-eastern cap of the Fermi bubbles at the same latitude is notably harder ($\alpha_{\rm PL} = -1.239 \pm 0.002$).

The radio fluxes in the outer halo show a harder spectrum compared with the gamma-ray flux for the outer outflows (for the north-eastern outer halo: $\alpha_{\rm r} = -1.07 \pm 0.04$, $\alpha_{\rm PL} = -1.499 \pm 0.004$; for the south-eastern outer halo: $\alpha_{\rm r} = -1.14 \pm 0.11$, $\alpha_{\rm PL} = -1.415 \pm 0.006$). But we need to note that the γ-ray emission is influenced by the KN effect at higher energy, which would result in a softer spectrum because of the suppressed cross section for the IC process[74]. Therefore, we need to check if the radio and γ-ray flux densities could be fitted with one single power-law electron distribution in the SED fitting. As shown in Supplementary Table 1b, the SED fitted magnetic field strength and electron indices based on Platz+[17] and Fermi14yr[66] are consistent for all the fittings within error range.

We can verify the magnetic field obtained based on the SED fitting as follows. The typical IC photon energy radiated by an electron with energy $E_{\rm e}$, up-scattering a photon of energy ϵ, can be given by $E_{\rm IC} \approx 3(E_{\rm e}/40\,{\rm GeV})^2(\epsilon/0.4\,{\rm eV})\,{\rm GeV}$, given that the KN effect is not important. The same electron radiates synchrotron photons in the magnetic field B at a typical energy of $E_{\rm syn} = 10^{-4}(E_{\rm e}/40\,{\rm GeV})^2(B/1\,\mu{\rm G})\,{\rm eV}$. Combing this two formulae, we get

$$E_{\rm IC} \approx 3(E_{\rm syn}/10^{-4}\,{\rm eV})(B/1\,\mu{\rm G})^{-1}(\epsilon/0.4\,{\rm eV})\,{\rm GeV}. \quad (12)$$

On the other hand, the synchrotron-to-IC flux ratio is $F_{\rm syn}/F_{\rm IC} = u_{\rm B}/u_{\rm ph}$. Here, $u_{\rm B}$ is the energy density for magnetic field and $u_{\rm ph}$ is the energy density for the seed photon field. Taking the north outer outflow for instance, the γ-ray flux at 3 GeV is measured to be about $10^{-9}\,{\rm erg\,s^{-1}\,cm^{-2}\,sr^{-1}}$, and the radio flux at 10^{-4} eV is about $4 \times 10^{-10}\,{\rm erg\,s^{-1}\,cm^{-2}\,sr^{-1}}$. For a soft electron spectrum, the optical radiation field is the dominant target radiation field for the IC radiation at 3 GeV, at which energy the KN effect is not important. Thus, for $u_{\rm ph} = 0.23\,{\rm eV\,cm^{-3}}$ and $\epsilon \approx 0.4$ eV, we obtain $B \approx 1.9\,\mu$G via equation (12), which is consistent with the fitting result.

The magnetic field strength we obtained for the southern cap of Fermi bubbles of $B \approx 1\,\mu$G is smaller than the magnetic field measurements for the Fermi bubbles at lower Galactic latitude[22,23,30]. This is expected because the magnetic field strength is expected to decrease when we measure medium higher in the Galactic halo.

We calculate the cooling time for the non-thermal radiations from the electron at the energy $E_{\rm e}$ (ref. 75) on the basis of the following equation considering the synchrotron cooling time $\tau_{\rm syn}$ and the IC cooling time $\tau_{\rm IC}$:

$$\begin{aligned}\tau_{\rm cool} &= \left(\tau_{\rm syn}^{-1} + \tau_{\rm IC}^{-1}\right)^{-1} \\ &\approx 5 \times 10^8 \left(\frac{E_{\rm e}}{1\,{\rm GeV}}\right)^{-1} \left(\frac{U_{\rm B}+U_{\rm ph}}{10^{-12}\,{\rm erg\,cm^{-3}}}\right)^{-1} {\rm yr},\end{aligned} \quad (13)$$

where $U_{\rm B} \equiv \frac{B^2}{8\pi}$ is the magnetic energy and $U_{\rm ph}$ is the energy density for the radiation field relevant to the IC process. The relativistic Bremsstrahlung is negligible in our analysis because the gas density in the halo is too low and the corresponding cooling time is more than 10 Gyr.

Outer outflow modelling

Regions with a star formation rate surface density larger than $0.01\,{\rm M_\odot\,yr^{-1}\,kpc^{-2}}$ drive superwinds that can become galactic outflows of speed of ~100–1,000 km s^{-1} (refs. 33,34,36,76). Extended Data Fig. 8 shows the star formation rate density of the Milky Way's disk as measured with Herschel telescope data[32]. We find that there are several clumps that have a sufficient star formation rate to drive galactic winds and that are at and about the star-forming ring located at 3–5 kpc from the GC.

The energy injection rate in the outer halo can be estimated as

$$E_{\rm tot} \approx \dot{E}_{\rm inj}\,\min\{t_{\rm dyn}, t_{\rm therm,cool}\}, \quad (14)$$

where $E_{\rm tot}$ is the total energy in the outer halo, $t_{\rm dyn}$ is the dynamical time scale of the outer halo and $t_{\rm therm,cool}$ is the cooling time of the hot plasma. The quantity $\dot{E}_{\rm inj}$ is the energy injection rate into the system. The system energy depends on the system time before the cooling is dominant, while it depends on the cooling time when it is shorter than the age of the outer halo ($t_{\rm dyn} > t_{\rm therm,cool}$). The cooling time for the hot plasma in the eROSITA bubbles is estimated at approximately 2×10^8 yr (ref. 5).

The total energy injection is made up of (1) the thermal energy of the hot plasma ($\dot{E}_{\rm therm}$), (2) the energy of non-thermal electrons ($\dot{E}_{\rm CR}$) and (3) the magnetic field energy ($\dot{E}_{\rm B}$). The energy in the hot thermal plasma that emits the X-ray halo is summarized in Extended Data Table 1 and is estimated depending on the bubbles' height (see Supplementary Information for more details). The CR energy can be derived from the electron energy distribution of the patch R1 SED fitting, which gives 2.2×10^{53} erg. If we assume that the same electron energy density resides in the rest of the outer eROSITA bubbles, the total relativistic CR energy would be 1.2×10^{55} erg. The magnetic energy can be estimated by $E_{\rm B} = VB^2/8\pi$, where V is the volume of the outer outflows. In our calculations for the energy of the halos below, we adopt a reasonable height ranging from 4 to 10 kpc. From our SED fitting, the magnetic strength at a height of 3 kpc is 1–2 μG. Assuming an average magnetic field strength of 3 μG across the entire outer outflows, the magnetic field energy is reported in Extended Data Table 1.

The injection rate of the dynamical energy in the wind can be expressed by

$$\dot{E}_{\rm inj} = \frac{1}{2}\dot{M}_{\rm inj}v_{\rm w}^2, \quad (15)$$

where $\dot{M}$ is the mass injection rate due to the Galactic outflows from the star-forming clumps and $v_{\rm w}$ is the velocity of the Galactic wind. We consider that the ions and electrons downstream have reached the same temperature T_g. The value of $v_{\rm w}$ can be estimated using the Rankine–Hugoniot relation

$$T_{\rm g} = \frac{3}{16}\frac{m_{\rm H}}{k_{\rm B}}(v_{\rm w} - v_{\rm g})^2, \quad (16)$$

where the quantity $m_{\rm H}$ is the mass of hydrogen and the quantity $v_{\rm g}$ is the velocity of the shock-heated gas. For a temperature of 0.3 keV (ref. 5) and $v_{\rm g} \ll v_{\rm w}$ for the outflows, the wind velocity is around $v_{\rm w} \approx 400\,{\rm km\,s^{-1}}$. The wind velocity substantially exceeds the sound speed in the hot wind, which is $c_{\rm s} \approx 180\,{\rm km\,s^{-1}}$. Thus, a termination shock is expected in the outer outflows.

A number of previous works reported a range of the supernova rate in the Milky Way of 2–6 per century[77–81]. The Herschel measurements for the star-forming rate of the Milky Way[32] show that a considerable amount of star-forming activity occurs in the 3–5-kpc star-forming ring of the Galaxy. Hence, the rate of supernovae at and about the 3–5-kpc star-forming ring can be approximated as 1 per century. The ejected energy of a supernova explosion is ~10^{51} erg (ref. 82). This corresponds to an energy injection rate from the 3–5-kpc star-forming ring of $\dot{E}_{\rm SFR} \approx 3.2 \times 10^{41}\,{\rm erg\,s^{-1}}$.

On the basis of our estimate of the height of magnetic ridges and the non-thermal electron cooling time scale (see Main text), we test outer outflows with heights of 4–10 kpc and system time of 10^8 and 10^9 yr, and summarize the results in Extended Data Table 1. Our calculations

show that the total energy in the outer halo is $8–20 \times 10^{55}$ erg, similar to what was found in previous work[5]. The energy injection rate required for the outer outflows is a few times 10^{40} erg s^{-1}, which corresponds to only 5–21% of that produced by core-collapse supernova explosions in the 3–5-kpc star-forming ring, which hence can amply supply the outer outflows. The mass loss rate from the 3–5-kpc star-forming ring is 0.3–1.3 $M_\odot$ yr^{-1}. Hence, our conclusion here is that the bulk of the multi-wavelength emission related to the outer halo can result from the Galactic outflows powered by the star-forming ring of our Milky Way located 3–5 kpc from the GC.

Our model provides an explanation for the bulk of the extended thermal and non-thermal emitting structures, as well as the magnetic field direction we measured. Nevertheless, there are some other phenomena of the Milky Way's outflows that need further investigation. For example, the North Polar Spur (NPS), the extended ridge structure extending up to 80° in latitude in the northeastern Galactic sky, is observed to have enhanced brightness compared with its southern counterpart. As demonstrated in Fig. 5, the magnetic ridges in the NPS are connected to the near end of the Galactic Bar, hence the density of the plasma can be more influenced in the NPS by violent star-forming activities. The X-ray surface brightness is proportional to the density squared of the emitting hot plasma, hence a slight intrinsic variation to the density results in a substantial change to the surface brightness. Moreover, previous research[83] has proposed that the metallicity of galactic outflows can vary owing to either previous active galactic nucleus events or starburst activities at the GC. Earlier X-ray research has studied the metallicity of the hot plasma in various patches of the Fermi and eROSITA bubbles and drawn different conclusions (sub-solar[30,84] or super-solar[85]). Indeed, at such low X-ray temperatures, it is basically impossible to detect the intrinsic continuum (Bremsstrahlung) at charge-coupled device (CCD) resolution, therefore abundances are unreliable. Additionally, the abundances will be characteristic of the ambient medium that has been shock heated, therefore it is logical that the abundances are assumed to be as low as the one of the Galactic halo. More studies on detailed simulations and observations for galactic outflows are needed to answer these questions.

Three-dimensional geometry of outer outflows

The eROSITA bubbles appear as two gigantic spheres extending up to more than 80° in latitude. We argue that the caps of the bubbles at such a high latitude can be reproduced by different intrinsic three-dimensional geometries. We have tested the X-ray-emitting structures with a height from 4 to 100 kpc using an open 'bouquet' shape in Extended Data Fig. 9. The bubble shape can even be reproduced with open outer outflows at an unrealistic height (H = 100 kpc; Extended Data Fig. 9d). Therefore, our modelling is consistent with the observation ('bubble shape') because of the projection effect.

Data availability

We use the following surveys in our paper to analyse the magnetic halo: synchrotron and dust data (https://lambda.gsfc.nasa.gov/), Fermi gamma-ray data (https://fermi.gsfc.nasa.gov/ssc/data/access/lat/14yr_catalog/), 3D dust extinction map (https://astro.acri-st.fr/gaia_dev/about) and the ROSAT all-sky survey (https://cade.irap.omp.eu/dokuwiki/doku.php?id=rass). The other data are taken from the maps of published papers, for which we provide references in the Supplementary Information.

Code availability

The following software and code packages have been used in our analysis: Python (https://www.python.org/) with the packages Numpy (https://numpy.org/), Healpy (https://healpy.readthedocs.io/), Astropy (https://www.astropy.org/) and Fermipy (https://fermipy.readthedocs.io/); Jupyter Notebook (https://jupyter-notebook.readthedocs.io/), Matplotlib (https://matplotlib.org/); and DS9 (https://sites.google.com/cfa.harvard.edu/saoimageds9). The package naima (https://naima.readthedocs.io/) is used to model the multi-wavelength results. The electron distribution is from the package ymw16 (https://www.atnf.csiro.au/research/pulsar/ymw16/). The JF12 magnetic field model comes from the package CRPropa (https://crpropa.github.io/CRPropa3/api/classcrpropa_1_1PlanckJF12bField.html).

References

1. Strickland, D. K., Heckman, T. M., Colbert, E. J. M., Hoopes, C. G. & Weaver, K. A. A high spatial resolution X-ray and Hα study of hot gas in the halos of star-forming disk galaxies. I. Spatial and spectral properties of the diffuse X-ray emission. *Astrophys. J. Suppl. Ser.* **151**, 193–236 (2004).
2. Strickland, D. K. & Heckman, T. M. Iron line and diffuse hard X-ray emission from the starburst galaxy M82. *Astrophys. J.* **658**, 258–281 (2007).
3. Krause, M. et al. CHANG-ES. XXII. Coherent magnetic fields in the halos of spiral galaxies. *Astron. Astrophys.* **639**, A112 (2020).
4. Krause, M. Magnetic fields and halos in spiral galaxies. *Galaxies* https://doi.org/10.3390/galaxies7020054 (2019).
5. Predehl, P. et al. Detection of large-scale X-ray bubbles in the Milky Way halo. *Nature* **588**, 227–231 (2020).
6. Hinshaw, G. et al. Nine-year Wilkinson Microwave Anisotropy Probe (WMAP) observations: cosmological parameter results. *Astrophys. J. Suppl. Ser.* https://doi.org/10.1088/0067-0049/208/2/19 (2013).
7. Vidal, M., Dickinson, C., Davies, R. D. & Leahy, J. P. Polarized radio filaments outside the Galactic plane. *Mon. Not. R. Astron. Soc.* **452**, 656–675 (2015).
8. Carretti, E. et al. Giant magnetized outflows from the centre of the Milky Way. *Nature* **493**, 66–69 (2013).
9. Wolleben, M. et al. The global magneto-ionic medium survey: a Faraday depth survey of the northern sky covering 1280–1750 MHz. *Astron. J.* https://doi.org/10.3847/1538-3881/abf7c1 (2021).
10. Liu, W. et al. The structure of the local hot bubble. *Astrophys. J.* https://doi.org/10.3847/1538-4357/834/1/33 (2017).
11. Berkhuijsen, E. M., Haslam, C. G. T. & Salter, C. J. Are the galactic loops supernova remnants? *Astron. Astrophys.* **14**, 252–262 (1971).
12. Lallement, R. et al. Three-dimensional maps of interstellar dust in the Local Arm: using Gaia, 2MASS, and APOGEE-DR14. *Astron. Astrophys.* **616**, A132 (2018).
13. Sofue, Y. The North Polar Spur and Aquila Rift. *Mon. Not. R. Astron. Soc.* **447**, 3824–3831 (2015).
14. Burn, B. J. On the depolarization of discrete radio sources by Faraday dispersion. *Mon. Not. R. Astron. Soc.* **133**, 67–83 (1966).
15. Sokoloff, D. D. et al. Depolarization and Faraday effects in galaxies. *Mon. Not. R. Astron. Soc.* **299**, 189–206 (1998).
16. Lallement, R. North Polar Spur/Loop I: gigantic outskirt of the Northern Fermi bubble or nearby hot gas cavity blown by supernovae? *Comp. Rend. Phys.* **23**, 1–24 (2023).
17. Scheel-Platz, L. I. et al. Multicomponent imaging of the Fermi gamma-ray sky in the spatio-spectral domain. *Astron. Astrophys.* **680**, A2 (2023).
18. Dobler, G., Finkbeiner, D. P., Cholis, I., Slatyer, T. & Weiner, N. The Fermi haze: a gamma-ray counterpart to the microwave haze. *Astrophys. J.* **717**, 825–842 (2010).
19. Planck Collaboration. et al. Planck intermediate results. IX. Detection of the Galactic haze with Planck. *Astron. Astrophys.* **554**, A139 (2013).
20. Lacki, B. C. The Fermi bubbles as starburst wind termination shocks. *Mon. Not. R. Astron. Soc.* **444**, L39–L43 (2014).
21. Crocker, R. M., Bicknell, G. V., Taylor, A. M. & Carretti, E. A unified model of the Fermi bubbles, microwave haze, and polarized radio lobes: reverse shocks in the Galactic Center's giant outflows. *Astrophys. J.* https://doi.org/10.1088/0004-637X/808/2/107 (2015).

22. Su, M., Slatyer, T. R. & Finkbeiner, D. P. Giant gamma-ray bubbles from Fermi-LAT: active galactic nucleus activity or bipolar galactic wind? *Astrophys. J.* **724**, 1044–1082 (2010).
23. Ackermann, M. et al. The spectrum and morphology of the Fermi bubbles. *Astrophys. J.* https://doi.org/10.1088/0004-637X/793/1/64 (2014).
24. Remazeilles, M., Dickinson, C., Banday, A. J., Bigot-Sazy, M. A. & Ghosh, T. An improved source-subtracted and destriped 408-MHz all-sky map. *Mon. Not. R. Astron. Soc.* **451**, 4311–4327 (2015).
25. Wolleben, M., Landecker, T. L., Reich, W. & Wielebinski, R. An absolutely calibrated survey of polarized emission from the northern sky at 1.4 GHz. Observations and data reduction. *Astron. Astrophys.* **448**, 411–424 (2006).
26. Rubiño-Martín, J. A. et al. QUIJOTE scientific results – IV. A northern sky survey in intensity and polarization at 10–20 GHz with the multifrequency instrument. *Mon. Not. R. Astron. Soc.* **519**, 3383–3431 (2023).
27. Fuskeland, U., Wehus, I. K., Eriksen, H. K. & Næss, S. K. Spatial variations in the spectral index of polarized synchrotron emission in the 9 yr WMAP sky maps. *Astrophys. J.* https://doi.org/10.1088/0004-637X/790/2/104 (2014).
28. Planck Collaboration. et al. Planck 2018 results. IV. Diffuse component separation. *Astron. Astrophys.* **641**, A4 (2020).
29. Ajello, M. et al. Fermi Large Area Telescope performance after 10 years of operation. *Astrophys. J. Suppl. Ser.* https://doi.org/10.3847/1538-4365/ac0ceb (2021).
30. Kataoka, J. et al. Suzaku Observations of the Diffuse X-Ray Emission across the Fermi Bubbles' Edges. *Astrophys. J.* **779**, 57 (2013).
31. Locatelli, N. et al. The warm–hot circumgalactic medium of the Milky Way as seen by eROSITA. *Astron. Astrophys.* **681**, A78 (2024).
32. Elia, D. et al. The star formation rate of the Milky Way as seen by Herschel. *Astrophys. J.* **941**, 162 (2022).
33. Chevalier, R. A. & Clegg, A. W. Wind from a starburst galaxy nucleus. *Nature* **317**, 44–45 (1985).
34. Heckman, T. M., Lehnert, M. D., Strickland, D. K. & Armus, L. Absorption-line probes of gas and dust in galactic superwinds. *Astrophys. J. Suppl. Ser.* **129**, 493–516 (2000).
35. Veilleux, S., Cecil, G. & Bland-Hawthorn, J. Galactic winds. *Annu. Rev. Astron. Astrophys.* **43**, 769–826 (2005).
36. Strickland, D. K. & Heckman, T. M. Supernova feedback efficiency and mass loading in the starburst and galactic superwind exemplar M82. *Astrophys. J.* **697**, 2030–2056 (2009).
37. Vink, J. & Yamazaki, R. A critical shock Mach number for particle acceleration in the absence of pre-existing cosmic rays: $M = \sqrt{5}$. *Astrophys. J.* **780**, 125 (2014).
38. Guo, X., Sironi, L. & Narayan, R. Electron heating in low Mach number perpendicular shocks. II. Dependence on the pre-shock conditions. *Astrophys. J.* **858**, 95 (2018).
39. Nguyen, D. D. & Thompson, T. A. Galactic winds and bubbles from nuclear starburst rings. *Astrophys. J. Lett.* **935**, L24 (2022).
40. Marasco, A. & Fraternali, F. Modelling the HI halo of the Milky Way. *Astron. Astrophys.* **525**, A134 (2011).
41. Faerman, Y., Sternberg, A. & McKee, C. F. Massive warm/hot galaxy coronae as probed by UV/X-ray oxygen absorption and emission. I. Basic model. *Astrophys. J.* **835**, 52 (2017).
42. Sancisi, R., Fraternali, F., Oosterloo, T. & van Moorsel, G.Funes, J. G. & Corsini, E. M. The vertical structure and kinematics of HI in spiral galaxies. In *Galaxy Disks and Disk Galaxies* (eds Funes, J. G. & Corsini, E. M.), vol. 230 of *Astronomical Society of the Pacific Conference Series*, 111–118 (2001).
43. Marasco, A., Marinacci, F. & Fraternali, F. On the origin of the warm–hot absorbers in the Milky Way's halo. *Mon. Not. R. Astron. Soc.* **433**, 1634–1647 (2013).
44. Meliani, Z. et al. The galactic bubbles of starburst galaxies. The influence of galactic large-scale magnetic fields. *Astron. Astrophys.* **683**, A178 (2024).
45. Sofue, Y. et al. Galactic Centre hypershell model for the North Polar Spurs. *Mon. Not. R. Astron. Soc.* **459**, 108–120 (2016).
46. Sofue, Y. & Kataoka, J. Interaction of the galactic-centre super bubbles with the gaseous disc. *Mon. Not. R. Astron. Soc.* **506**, 2170–2180 (2021).
47. Yang, H. Y. K., Ruszkowski, M. & Zweibel, E. G. Fermi and eROSITA bubbles as relics of the past activity of the Galaxy's central black hole. *Nat. Astron.* **6**, 584–591 (2022).
48. Mou, G. et al. Asymmetric eROSITA bubbles as the evidence of a circumgalactic medium wind. *Nat. Commun.* **14**, 781 (2023).
49. Sarkar, K. C. Possible connection between the asymmetry of the North Polar Spur and Loop I and Fermi bubbles. *Mon. Not. R. Astron. Soc.* **482**, 4813–4823 (2019).
50. Snowden, S. L. et al. ROSAT survey diffuse X-ray background maps. II. *Astrophys. J.* **485**, 125–135 (1997).
51. Maconi, E. et al. Modelling local bubble analogs: synthetic dust polarization maps. *Mon. Not. R. Astron. Soc.* **523**, 5995–6010 (2023).
52. Frisch, P. C., Redfield, S. & Slavin, J. D. The interstellar medium surrounding the Sun. *Annu. Rev. Astron. Astrophys.* **49**, 237–279 (2011).
53. Yeung, M. C. H. et al. SRG/eROSITA X-ray shadowing study of giant molecular clouds. *Astron. Astrophys.* **676**, A3 (2023).
54. Beck, R. Magnetic fields in spiral galaxies. *Astron. Astrophys. Rev.* **24**, 4 (2015).
55. Bennett, C. L. et al. Nine-year Wilkinson Microwave Anisotropy Probe (WMAP) observations: final maps and results. *Astrophys. J. Suppl. Ser.* **208**, 20 (2013).
56. Ehle, M. & Beck, R. Ionized gas and intrinsic magnetic fields in the spiral galaxy NGC 6946. *Astron. Astrophys.* **273**, 45–64 (1993).
57. Armstrong, J. W., Rickett, B. J. & Spangler, S. R. Electron density power spectrum in the local interstellar medium. *Astrophys. J.* **443**, 209 (1995).
58. Chepurnov, A. & Lazarian, A. Extending the big power law in the sky with turbulence spectra from Wisconsin Hα Mapper data. *Astrophys. J.* **710**, 853–858 (2010).
59. Yao, J. M., Manchester, R. N. & Wang, N. A new electron-density model for estimation of pulsar and FRB distances. *Astrophys. J.* **835**, 29 (2017).
60. Jansson, R. & Farrar, G. R. The Galactic magnetic field. *Astrophys. J. Lett.* **761**, L11 (2012).
61. Planck Collaboration. et al. Planck intermediate results. XLII. Large-scale Galactic magnetic fields. *Astron. Astrophys.* **596**, A103 (2016).
62. Carretti, E. et al. S-band Polarization All-Sky Survey (S-PASS): survey description and maps. *Mon. Not. R. Astron. Soc.* **489**, 2330–2354 (2019).
63. Testori, J. C., Reich, P. & Reich, W. A fully sampled λ21 cm linear polarization survey of the southern sky. *Astron. Astrophys.* **484**, 733–742 (2008).
64. Iacobelli, M. et al. Studying Galactic interstellar turbulence through fluctuations in synchrotron emission. First LOFAR Galactic foreground detection. *Astron. Astrophys.* **558**, A72 (2013).
65. Abeysekara, A. U. et al. Extended gamma-ray sources around pulsars constrain the origin of the positron flux at Earth. *Science* **358**, 911–914 (2017).
66. Abdollahi, S. et al. Incremental Fermi Large Area Telescope fourth source catalog. *Astrophys. J. Suppl. Ser.* **260**, 53 (2022).
67. Wood, M. et al. Fermipy: an open-source Python package for analysis of Fermi-LAT data. in *Proc. International Cosmic Ray Conference* (eds Y.-S. Kwak, Y.-S. et al.) https://doi.org/10.22323/1.301.0824 (SISSA Medialab, 2017).
68. Popescu, C. C. et al. A radiation transfer model for the Milky Way: I. Radiation fields and application to high-energy astrophysics. *Mon. Not. R. Astron. Soc.* **470**, 2539–2558 (2017).

69. Zabalza, V. naima: a Python package for inference of relativistic particle energy distributions from observed nonthermal spectra. in *Proc. International Cosmic Ray Conference 2015* (eds van den Berg, A. M. et al.) 922 (SISSA Medialab, 2015).
70. Aharonian, F. A., Kelner, S. R. & Prosekin, A. Y. Angular, spectral, and time distributions of highest energy protons and associated secondary gamma rays and neutrinos propagating through extragalactic magnetic and radiation fields. *Phys. Rev. D* **82**, 043002 (2010).
71. Khangulyan, D., Aharonian, F. A. & Kelner, S. R. Simple analytical approximations for treatment of inverse Compton scattering of relativistic electrons in the blackbody radiation field. *Astrophys. J.* **783**, 100 (2014).
72. Zirakashvili, V. N. & Aharonian, F. Analytical solutions for energy spectra of electrons accelerated by nonrelativistic shock-waves in shell type supernova remnants. *Astron. Astrophys.* **465**, 695–702 (2007).
73. Ackermann, M. et al. In-flight measurement of the absolute energy scale of the Fermi Large Area Telescope. *Astropart. Phys.* **35**, 346–353 (2012).
74. Blumenthal, G. R. & Gould, R. J. Bremsstrahlung, synchrotron radiation, and Compton scattering of high-energy electrons traversing dilute gases. *Rev. Mod. Phys.* **42**, 237–271 (1970).
75. Heesen, V., Dettmar, R.-J., Krause, M., Beck, R. & Stein, Y. Advective and diffusive cosmic ray transport in galactic haloes. *Mon. Not. R. Astron. Soc.* **458**, 332–353 (2016).
76. Heesen, V. The radio continuum perspective on cosmic-ray transport in external galaxies. *Astrophys. Space Sci.* **366**, 117 (2021).
77. Reed, B. C. New estimates of the solar-neighborhood massive star birthrate and the Galactic supernova rate. *Astron. J.* **130**, 1652–1657 (2005).
78. Diehl, R. et al. Radioactive ^{26}Al from massive stars in the Galaxy. *Nature* **439**, 45–47 (2006).
79. Li, W. et al. Nearby supernova rates from the Lick Observatory Supernova Search – III. The rate–size relation, and the rates as a function of galaxy Hubble type and colour. *Mon. Not. R. Astron. Soc.* **412**, 1473–1507 (2011).
80. Rozwadowska, K., Vissani, F. & Cappellaro, E. On the rate of core collapse supernovae in the milky way. *N. Astro.* **83**, 101498 (2021).
81. Adams, S. M., Kochanek, C. S., Beacom, J. F., Vagins, M. R. & Stanek, K. Z. Observing the next Galactic supernova. *Astrophys. J.* https://doi.org/10.1088/0004-637X/778/2/164 (2013).
82. Poznanski, D. An emerging coherent picture of red supergiant supernova explosions. *Mon. Not. R. Astron. Soc.* **436**, 3224–3230 (2013).
83. Inoue, Y. et al. Metal enrichment in the Fermi bubbles as a probe of their origin. *Publ. Astron. Soc. Jpn.* **67**, 56 (2015).
84. LaRocca, D. M. et al. An analysis of the North Polar Spur using HaloSat. *Astrophys. J.* https://doi.org/10.3847/1538-4357/abbdfd (2020).
85. Gupta, A., Mathur, S., Kingsbury, J., Das, S. & Krongold, Y. Thermal and chemical properties of the eROSITA bubbles from Suzaku observations. *Nat. Astron.* **7**, 799–804 (2023).
86. Fox, A. J. et al. The mass inflow and outflow rates of the Milky Way. *Astrophys. J.* https://doi.org/10.3847/1538-4357/ab40ad (2019).

Acknowledgements

H.S.Z. acknowledges support by the X-riStMAs project (Seal of Excellence no. 0000153) under the National Recovery and Resilience Plan (PNRR), Mission 4, Component 2, Investment 1.2 – Italian Ministry of University and Research, funded by the European Union – NextGenerationEU. H.S.Z. also acknowledges computing support from the PLEIADI supercomputer from INAF. H.S.Z., G.P., N.L., X.Z., Y.Z. and G.S. acknowledge financial support from the European Research Council (ERC) under the European Union's Horizon 2020 research and innovation program HotMilk (grant agreement no. 865637). G.P. also acknowledges support from Bando per il Finanziamento della Ricerca Fondamentale 2022 dell'Istituto Nazionale di Astrofisica (INAF): GO Large program and from the Framework per l'Attrazione e il Rafforzamento delle Eccellenze (FARE) per la ricerca in Italia (R20L5S39T9). M.R.M. acknowledges support from NASA under ADAP grant 80NSSC24K0639. The authors acknowledge X.Y. Li, X. Wu, M. Sasaki, G. Pareschi and G. Ghisellini.

Author contributions

H.S.Z. and G.P. led the project. H.S.Z. performed the analysis. E.C., H.S.Z. and M.H. led the radio data analysis and magnetic field measurement. G.P., H.S.Z., N.L. and X.Z. led the X-ray study. R.Y.L., H.S.Z., F.A., H.M.Z., M.R.M., Y.Z. and G.S. led the gamma-ray study. H.S.Z., G.P., E.C., R.Y.L. and M.R.M. led the multi-wavelength comparison and wrote the manuscript. All authors contributed to improving the analysis and the manuscript.

Competing interests

The authors declare no competing interests.

Additional information

Extended data is available for this paper at https://doi.org/10.1038/s41550-024-02362-0.

Supplementary information The online version contains supplementary material available at https://doi.org/10.1038/s41550-024-02362-0.

Correspondence and requests for materials should be addressed to He-Shou Zhang, Gabriele Ponti, Ettore Carretti, Ruo-Yu Liu or Mark R. Morris.

Peer review information *Nature Astronomy* thanks Jun Kataoka and the other, anonymous, reviewer(s) for their contribution to the peer review of this work.

Reprints and permissions information is available at www.nature.com/reprints.

Publisher's note Springer Nature remains neutral with regard to jurisdictional claims in published maps and institutional affiliations.

Springer Nature or its licensor (e.g. a society or other partner) holds exclusive rights to this article under a publishing agreement with the author(s) or other rightsholder(s); author self-archiving of the accepted manuscript version of this article is solely governed by the terms of such publishing agreement and applicable law.

© The Author(s), under exclusive licence to Springer Nature Limited 2024

[1]INAF Osservatorio Astronomico di Brera, Merate, Lecco, Italy. [2]Max-Planck-Institut für Extraterrestrische Physik, Garching bei München, Germany. [3]INAF Istituto di Radioastronomia, Bologna, Italy. [4]School of Astronomy and Space Science, Nanjing University, Nanjing, China. [5]Key Laboratory of Modern Astronomy and Astrophysics, Nanjing University, Nanjing, China. [6]Department of Physics and Astronomy, University of California, Los Angeles, CA, USA. [7]Department of Astrophysics/IMAPP, Radboud University Nijmegen, Nijmegen, The Netherlands. [8]Dublin Institute for Advanced Studies, Dublin, Ireland. [9]Max-Planck-Institut für Kernphysik, Heidelberg, Germany. [10]Yerevan State University, Yerevan, Armenia. [11]Guangxi Key Laboratory for Relativistic Astrophysics, School of Physical Science and Technology, Guangxi University, Nanning, China. [12]DiSAT, Università degli Studi dell'Insubria, Como, Italy. ✉e-mail: heshou.zhang@inaf.it; heshouzhang.astrophy@gmail.com; gabriele.ponti@inaf.it; carretti@ira.inaf.it; ryliu@nju.edu.cn; morris@astro.ucla.edu

https://doi.org/10.1038/s41550-024-02362-0

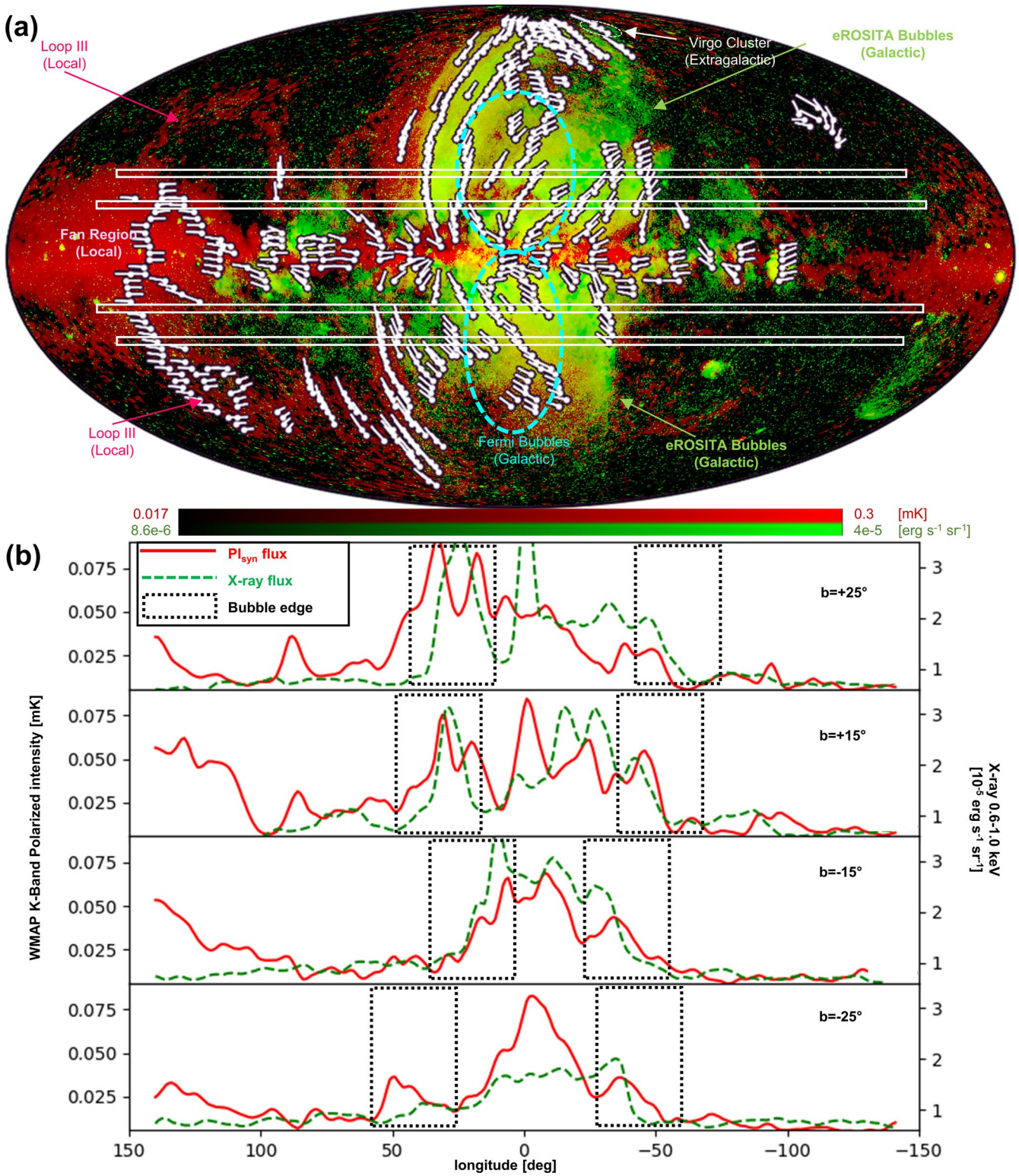

Extended Data Fig. 1 | Comparison between the X-ray surface brightness of the eROSITA all-sky map (0.6-1.0 keV) and the magnetic ridges. Panel (**a**) presents the magnetic ridges from Fig. 1(b), with four constant latitude cuts at the roots of the X-ray outer halos. The comparisons between the polarized intensity WMAP-K Band (ref. 6) (PI_{syn}, red) and the 0.6-1.0 keV eROSITA (ref. 5) X-ray emission (green) for the four cuts are presented in panel (**b**). The detected magnetic ridges are clear peaks of the red curves in (**b**). At the edges of the X-ray outer halo (highlighted in dotted boxes), the enhancements of the polarized synchrotron intensity ($PI_{syn,max}$) are observed with an offset of only a few degrees. While the large-scale magnetic structures surrounding the northern cap of the X-ray outer halo appear to largely enclose the Bubble, the same is not obviously true for the southern halo; there, only the southeastern magnetic ridge approaches the cap of the southern X-ray outer halo.

https://doi.org/10.1038/s41550-024-02362-0

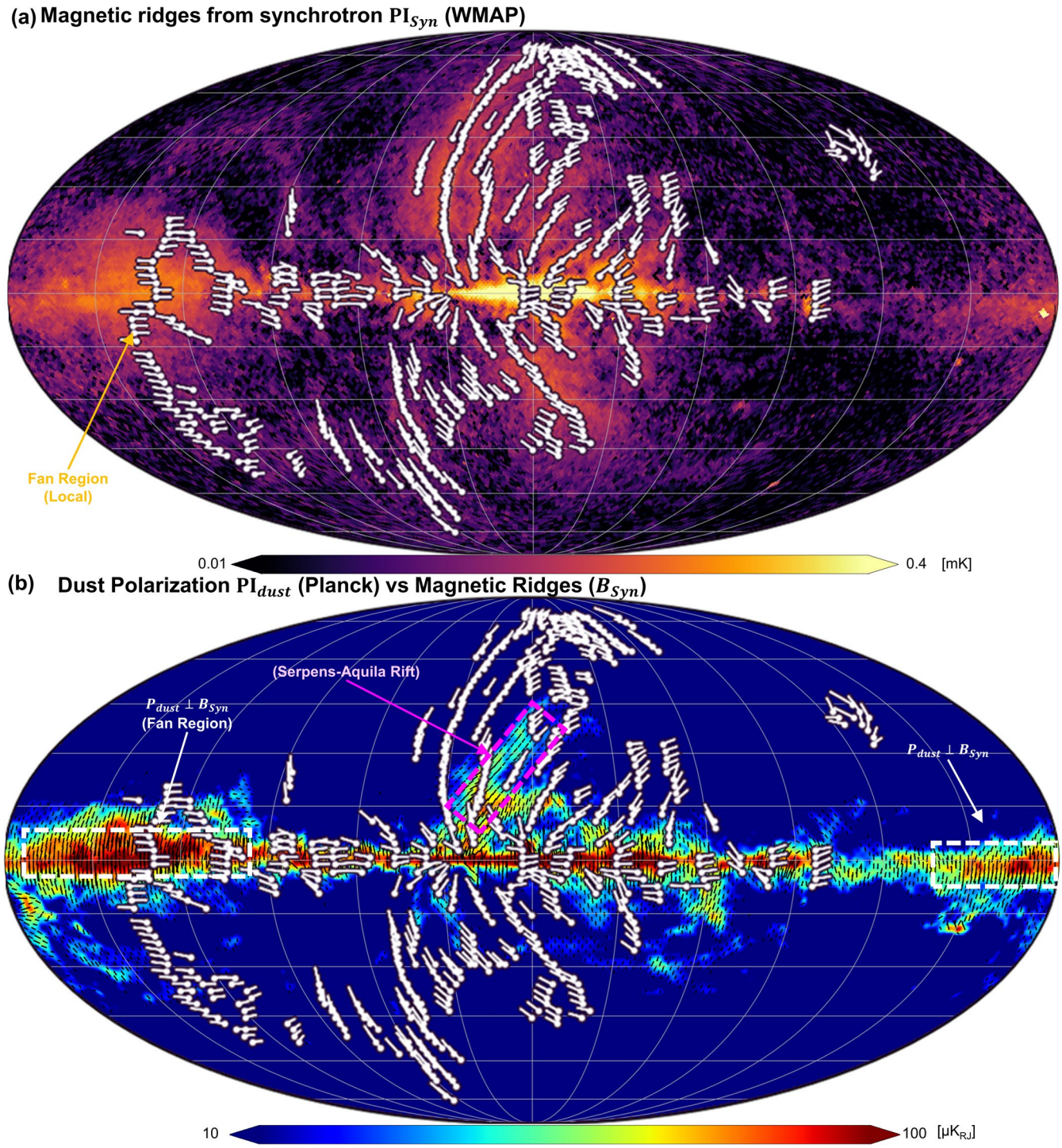

Extended Data Fig. 2 | Comparison between dust and synchrotron polarization. (**a**) Magnetic field ridges detected by synchrotron polarization (B_{syn}, WMAP at 22.8 GHz). The coherent ridges are enhanced in their polarized synchrotron intensity and connected by the magnetic field lines. (**b**) Comparison between the polarized emission of thermal dust (P_{Dust}, background black bars for direction and filled color for polarized intensity by Planck at 353 GHz from ref. 28) and the magnetic ridges deduced from synchrotron (white lines adapted from panel **a**). The polarized E-vectors of the dust emission shows a general perpendicular direction to the magnetic field from synchrotron in the Galactic plane ($|b| < 5°$), while some of the polarized E-vectors of dust emission is parallel to the magnetic field in the known local structure within the Serpens-Aquila Rift. However, most of the magnetic ridges presented in (**a**) have no dust counterparts, hence they are Galactic structures.

https://doi.org/10.1038/s41550-024-02362-0

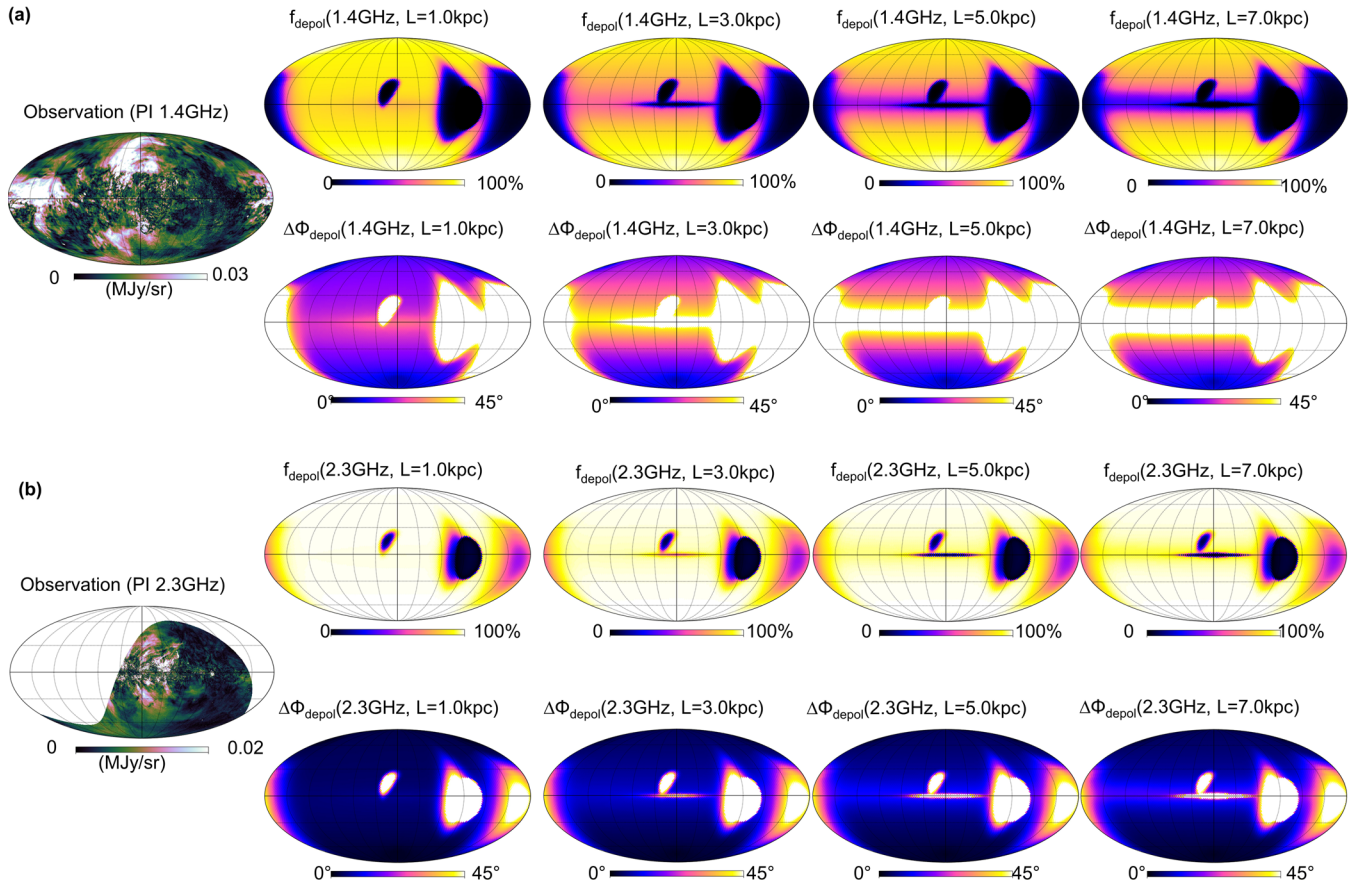

Extended Data Fig. 3 | Faraday depolarization by the turbulent Galactic magnetic field out to different distances from the Sun. The first column is the observed polarized emission at 1.4 GHz (**a**) and 2.3 GHz (**b**). Columns 2–5 show the Faraday depolarization f_{depol} and angle dispersion $\Delta\Phi$ due to the turbulent Galactic magnetic field, estimated as described in the Methods section. These maps represent the depolarization effects for polarized synchrotron radiations at distances of 1, 3, 5, and 7 kpc from us, shown at frequencies of 1.4 GHz (top two rows) and 2.3 GHz (bottom two rows), respectively. The white color in $\Delta\Phi$ maps indicates where the dispersion of polarization angles is expected to be more than 45°. At 1.4 GHz frequency, the depolarization screen shows notable growth in latitude between L = 1–5 kpc. The L = 5-kpc case matches well the observed depolarization and the emission at mid and high Galactic latitudes, and therefore the radiation from the magnetic ridges must arise at a distance beyond 5 kpc.

https://doi.org/10.1038/s41550-024-02362-0

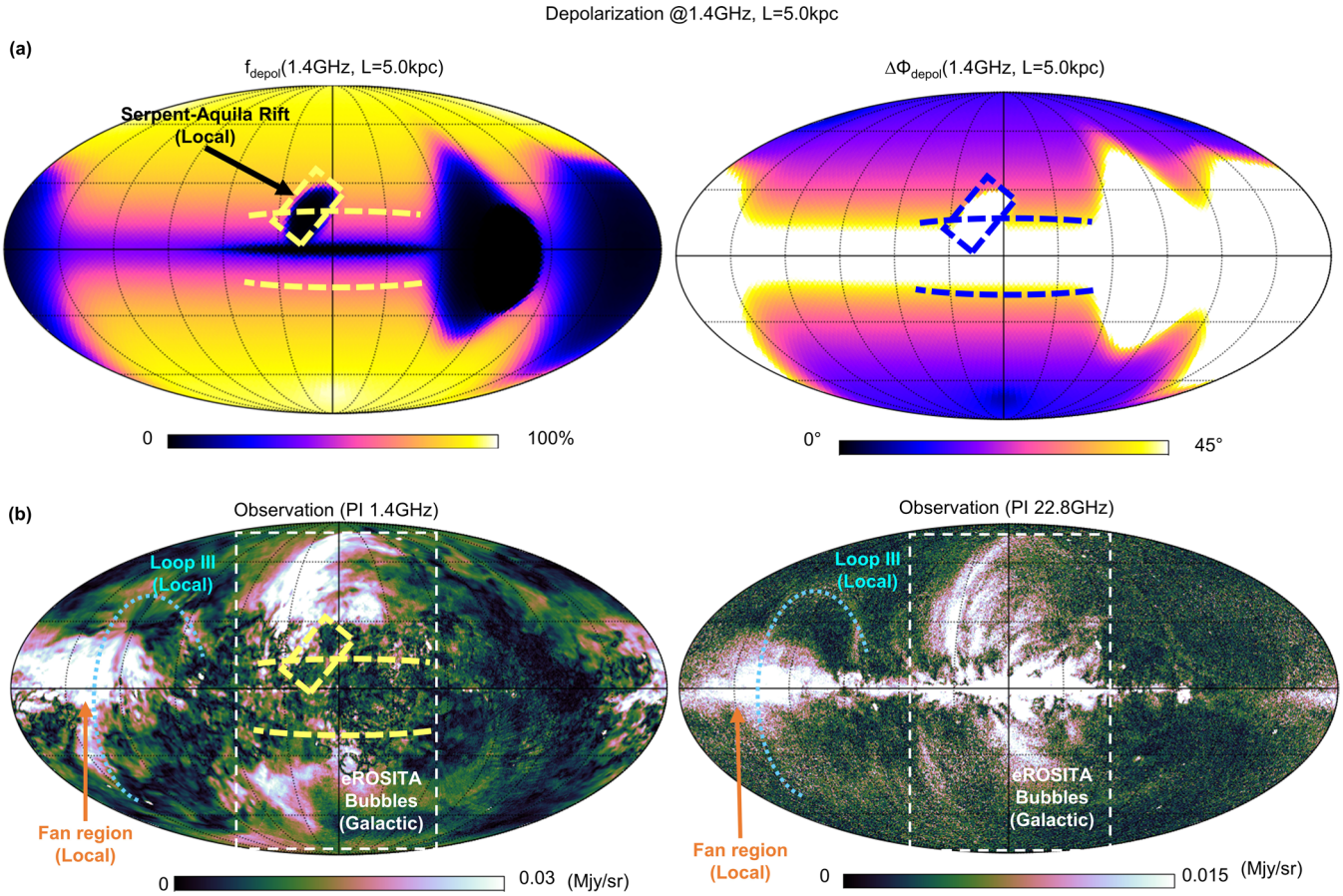

Extended Data Fig. 4 | Depolarization of the polarized radio emission ridges and local structures, such as the Fan region and Loop III. (**a**) Depolarization analyses (f_{depol}, $\Delta\Phi_{depol}$) at 1.4 GHz; (**b**) observations for polarized intensity at 1.4 GHz (refs. 25,63) and 22.8 GHz (refs. 6,55). No Faraday depolarization is expected for local emission down to the Galactic disc. At 1.4 GHz, the radio counterpart of the eROSITA Bubbles is depolarized at Galactic latitudes $|b| \lesssim 20°$, whilst no depolarization is observed for the Fan region or Loop III.

https://doi.org/10.1038/s41550-024-02362-0

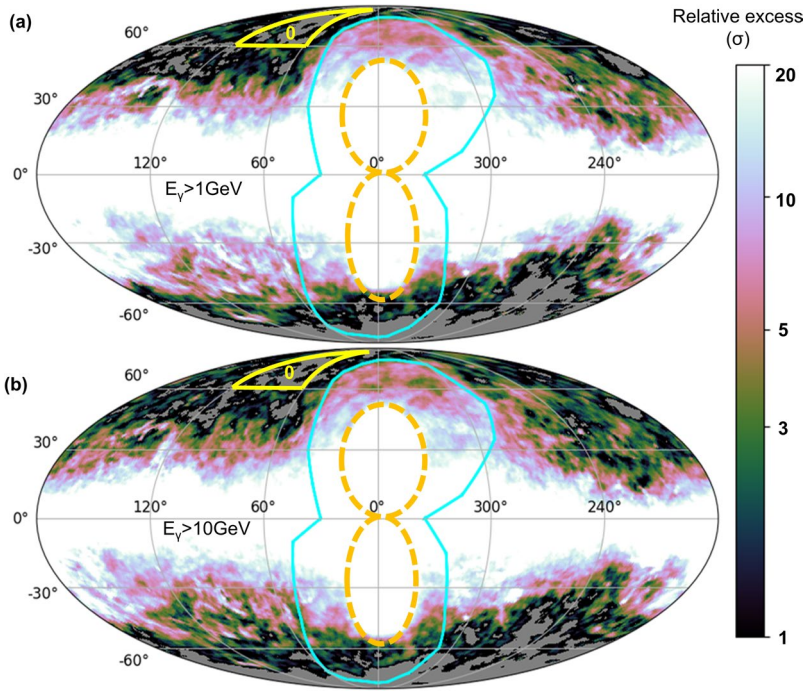

Extended Data Fig. 5 | γ − ray diffuse emission intensity maps. Following Fig. 4a and the calculations in Methods, we calculate the relative excess of the γ − ray flux density compared to patch R0 for γ − ray photons with (**a**) $E_\gamma \gtrsim 1$ GeV; (**b**) $E_\gamma \gtrsim 10$ GeV. The background area is selected in the yellow triangle in the northeast (the same as Patch R0 in Fig. 4a). The two lines are the edges of the eROSITA (solid) and Fermi (dashed) Bubbles.

https://doi.org/10.1038/s41550-024-02362-0

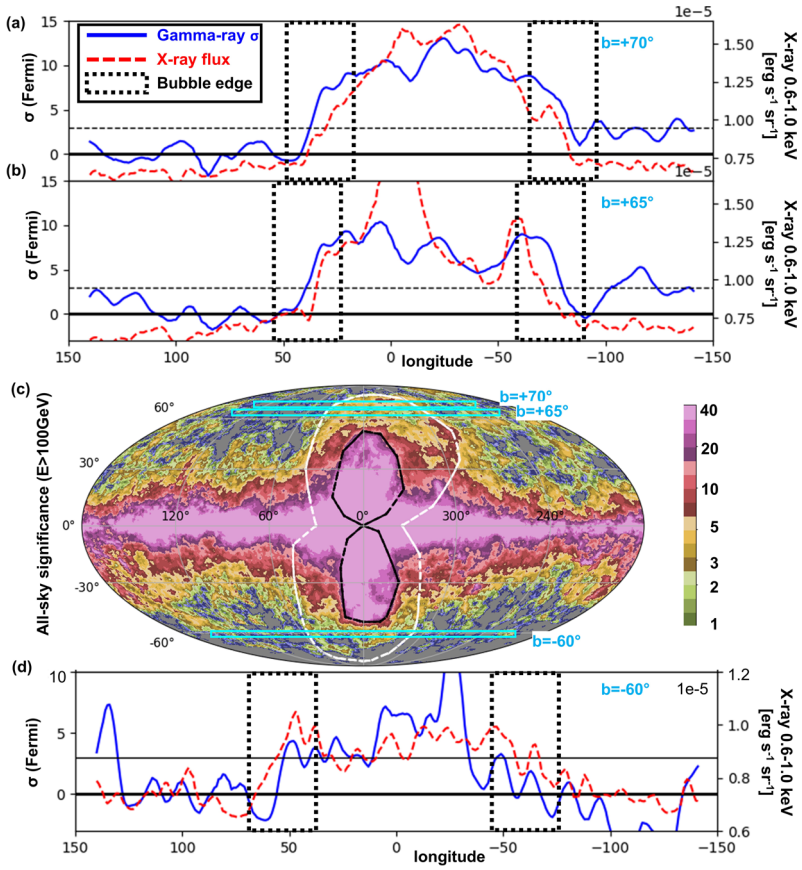

Extended Data Fig. 6 | Comparison between the X-ray surface brightness (0.6-1.0 keV) and gamma-ray intensity ($E_\gamma \geq 100$ GeV) at high Galactic latitudes. Two cuts are considered in the Galactic north for (**a**): $l = +70°$, (**b**): $l = +65°$, with X-ray (red dashed lines) and gamma-ray (blue lines). The all-sky significance map is shown in (**c**), where the span of cuts are marked. The cut in the Galactic south (**d**): $l = -60°$ is considered. Lower latitudes are not considered to avoid the influence of foreground structures or the Fermi Bubbles. The two energy bands have shown enhancements beyond the background within the edges of the X-ray outer halo, and the edges of the enhancements are in agreement with a separation of only a few degrees. The consistencies are observed in the southern cut, but the enhanced plateau is less evident for the southern Bubble.

https://doi.org/10.1038/s41550-024-02362-0

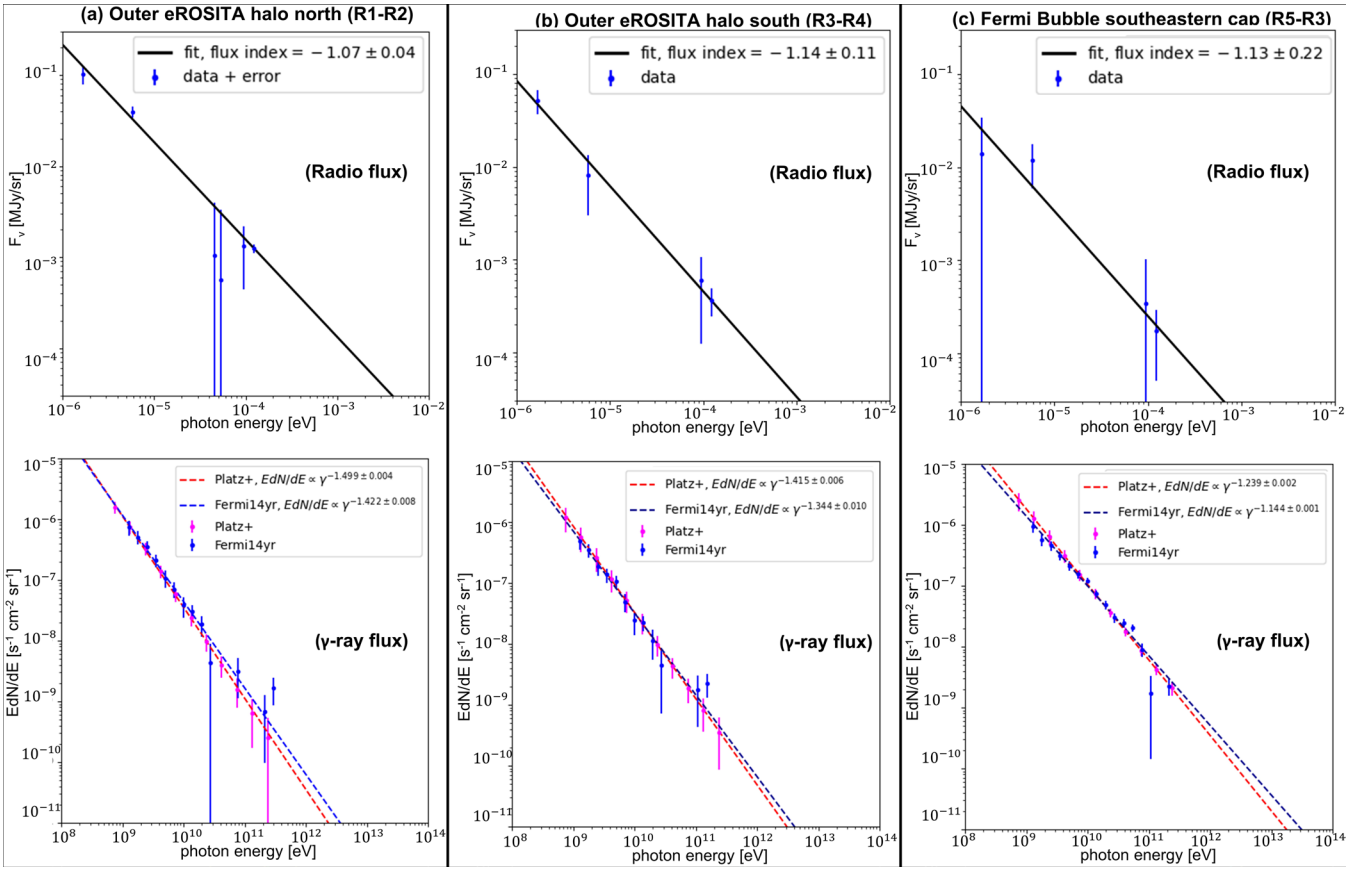

Extended Data Fig. 7 | Power-law fits for observed fluxes in radio and γ − ray bands. Upper plots fit the radio fluxes with respect to the energy $F_\nu \propto E_\gamma^{\alpha_r}$. Lower plots fit the gamma-ray fluxes with respect to the energy for Platz+ (ref. 17) − $EdN/dE \propto E_\gamma^{\alpha_{Platz}}$, Fermi14yr − $EdN/dE \propto E_\gamma^{\alpha_{F14}}$. The error-bars reported here for the gamma-ray data are based on the statistical uncertainties (see 'Data and errors for SED' in the Methods section for details). The reference frequencies are listed in the Supplementary Table 2. The error-bars reported for the radio fluxes are calculated based on the flux density calibration accuracy and beam sensitivity of the corresponding surveys, as defined in the Supplementary. The definitions of the fitting parameters are described 'Fitting results' in the Methods section. (**a**) northeastern outer outflows (R1-R2). $\alpha_r = -1.07 \pm 0.04$, $\alpha_{Pl} = -1.499 \pm 0.004$, and $\alpha_{F14} = -1.422 \pm 0.008$. (**b**) southeastern outer outflows (R3-R4). $\alpha_r = -1.14 \pm 0.11$, $\alpha_{Pl} = -1.415 \pm 0.006$, and $\alpha_{F14} = -1.344 \pm 0.010$. (**c**) southeastern Fermi Bubble cap (R5-R3). $\alpha_r = -1.13 \pm 0.22$, $\alpha_{Pl} = -1.239 \pm 0.002$, and $\alpha_{F14} = -1.144 \pm 0.001$.

https://doi.org/10.1038/s41550-024-02362-0

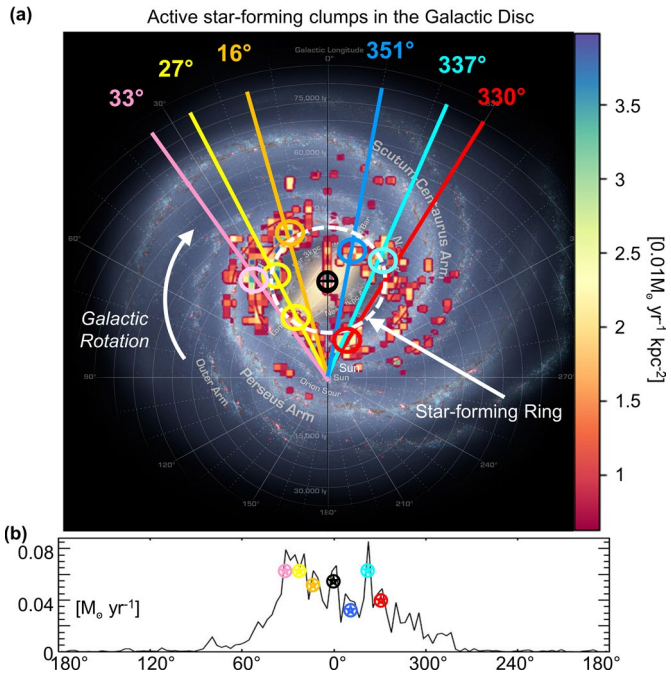

Extended Data Fig. 8 | Active star forming clumps. (**a**) an artist's view of the Galaxy (NASA/JPL-Caltech/R. Hurt) with the active star-forming clumps and their Galactic longitude overlaid. The specific star formation rates are measured from ref. 32 binned by a resolution of 0.5 × 0.5 kpc^2, and the clumps with $\Sigma_{SFR} \gtrsim 0.02\ M_\odot yr^{-1} kpc^{-2}$/bin are considered. (**b**) The footpoints of the magnetic ridges correspond to the marked clumps with a high star-formation rate on the Galactic plane (from measurements in the Fig. 4 of ref. 32).

https://doi.org/10.1038/s41550-024-02362-0

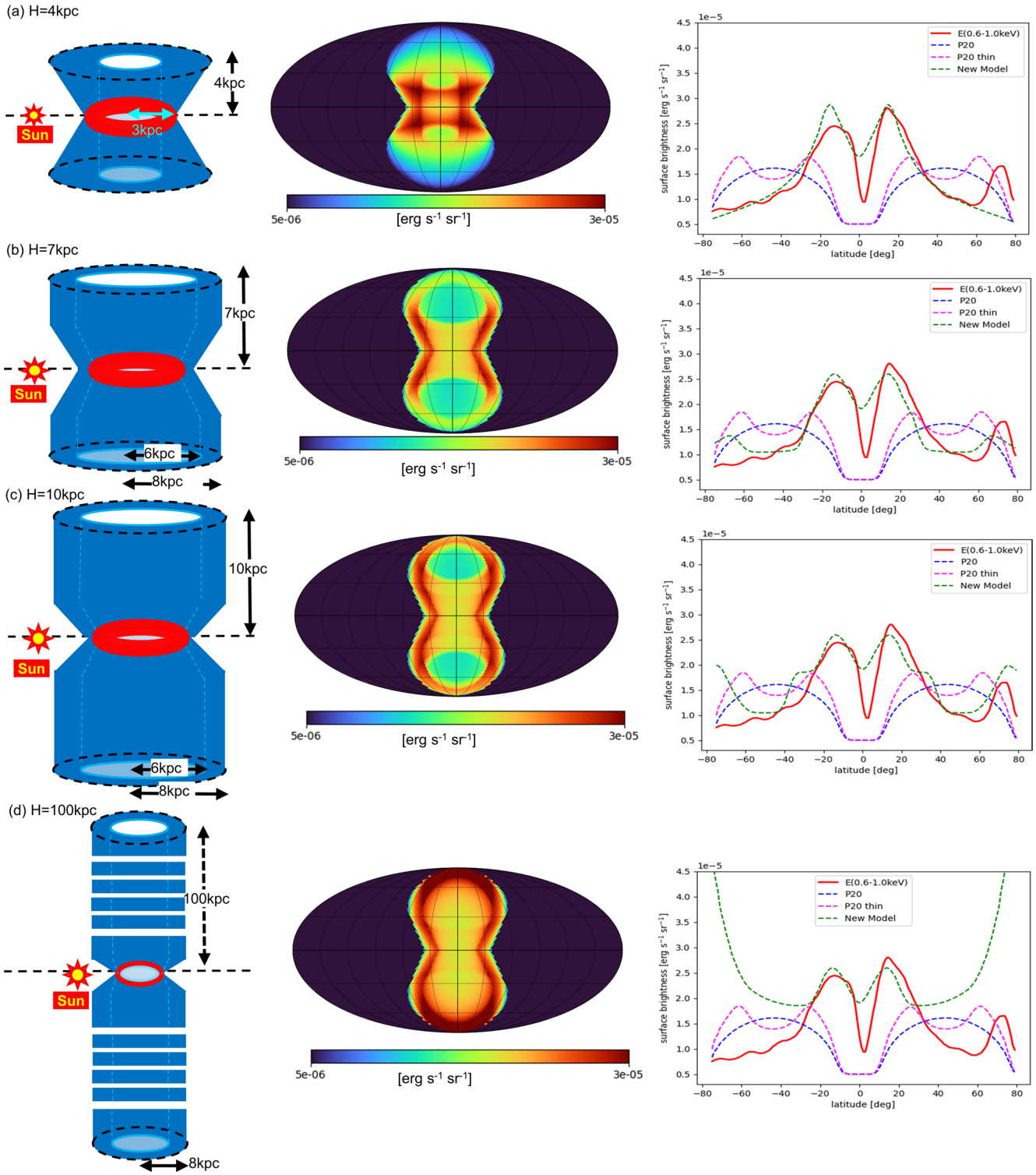

Extended Data Fig. 9 | Projection effect of the outer halo. The geometric check for the projection of an open 'bouquet' outer halo is presented with four different heights: (**a**) H = 4 kpc (having an inner vacant cylinder with bottom radius of 3 kpc); (**b**) H = 7 kpc (with a 2-kpc thickness); (**c**) H = 10 kpc (with a 2-kpc thickness); (**d**) H = 100 kpc (with a 2-kpc thickness). We assume that the density in the outer halo is uniform, the temperature and the metallicity in the outer outflow are T=0.3 keV, metallicity is 0.2 solar (refs. 5,30). Their corresponding projections are presented in the middle column. In the right column, cuts at western sky at $l = 330°$ for the three projections (green line) are compared with the observation (red, ref. 5), the '**P**20' model (blue) and '**P**20 thin' model (magenta). This figure shows that a 'bubble-shape' with cap can be reproduced by an open halo because of the projection effect. The intrinsic 3D structure of the X-ray emitting outer halo cannot be inferred from only a 2D projection.

https://doi.org/10.1038/s41550-024-02362-0

Extended Data Table 1 | Calculations for the outer outflows

Assumptions						
H_{sys} [kpc]	4		7		10	
t_{dyn} [yrs]	10^8	10^9	10^8	10^9	10^8	10^9
Results						
E_{therm} [$\times 10^{55}$ erg]	5.9		10		14	
E_B [$\times 10^{55}$ erg]	1.5		3.3		5.3	
E_{tot} [$\times 10^{55}$ erg]	8.6		15		21	
$\dot{E}_{inj}$ [$\times 10^{40}$ erg/s]	2.7	1.4	4.7	2.5	6.6	3.5
χ_{inj} [%]	8.5	4.5	14.6	7.7	20.5	10.8
$\dot{M}_{inj}$ [$M_\odot$/yr]	0.54	0.28	0.92	0.49	1.3	0.68

The quantities H_{sys} and t_{dyn} represent the assumed height and dynamical timescale of the outer halo, respectively. E_{therm} and E_B are the obtained energy of the outer halo for hot plasma and magnetic fields. The CR energy is obtained to be 1.2×10^{55} erg from SED analysis (Methods). E_{tot} is the total energy of the outer halo, which is at similar order of magnitude with a factor of a few difference compared to the energy estimated from ref. 5. The geometries of the system are adopted from Fig. 5c: plasma filled evenly in the outer shell with a vacant inner cylinder having 3 kpc bottoms radius. $\dot{E}_{inj}$ is the energy injection rate obtained from Equation (14) and $\chi_{inj} \equiv \dot{E}_{inj}/\dot{E}_{SFR}$ is the required percentage of the energy injection rate due to the supernova explosions from the star forming ring located 3–5 kpc from the GC in the Galactic disk (see Methods). $\dot{M}_{inj}$ is the mass injection rate obtained from Equation (15). *Our results show that the supernova explosions from the 3–5 kpc star forming ring are enough to fuel all the tested scenarios, and the mass injection rate is consistent with the measurements from* ref. 86.